

Science Forum (Journal of Pure and Applied Sciences)

SCIENCE FORUM

Journal Homepage: https://atbu.edu.ng/science-forum/

Structural and Mineral Exploration Study at Transition Zone of Mambilla Plateau and Environs, Northeastern Nigeria, Using Integrated Geophysical Data

Andarawus Yohanna ¹ Othniel Kamfani Likkason², Maigari Abubakar Sadiq³, Ali.S² Mohammed Aliyu Kaura¹, Josiah Nuhu Jabbo⁴

- ¹Department of Geology, Federal University of Lafia, P.M.B 1075, Nasarawa State, Nigeria
- ²Department of Physics, Abubakar Tafawa Balewa University Bauchi, P.M.B 1051, Bauchi State, Nigeria
- ³Department of Applied Geology, Abubakar Tafawa Balewa University Bauchi, P.M.B 1051, Bauchi State, Nigeria
- ⁴Department of Geological Technology, School of Science and Technology, Abubakar Tatari Ali Polytechnic Bauchi, Nigeria

ABSTRACT

To figure out the underground structures, the tectonic framework, and the minerals in the area., the transition zone of the Mambila Plateau and surroundings in northeastern Nigeria has been explored utilizing aeromagnetic, pseudo gravity, and landsat-8 remotely sensed. Several depth estimation and filtering methods, such as the first vertical derivative, total horizontal derivative, and total gradient, were used on the magnetic data (analytical signal), upward continuation, and pseudo gravity transform. Using landsat-8 imagery data, aeromagnetic, and pseudo gravity transforms, it was possible to identify mineral zones with hydrothermal changes, shallow and deep intrusive masses, buried faults, lineaments, and lithological units. A thorough field mapping revealed and confirmed a few mineralization zones with great potential. The mining areas exhibit high structural density, which highlights the value of lineaments density maps in identifying probable mineralization zones and the structures that regulate mineralization. The principal tectonic trends are NE-SW, NNE-SSW along with less significant NNW, WNW, NS, and NE trends, is shown by statistical trend analysis of the lineaments collected from geological, filtered magnetic, and density maps. The corresponding magnetic structures were scanned upward continuing at depths ranging from the surface to 3000m. Power spectrum and source parameter imaging approaches have been used to determine the depth of a structure. The results reveal that the average computed depth ranges from 1.2 km to 1.7 km, whereas the depth to volcanic intrusions ranges from 0.345 km to 0.461 km.

ARTICLE INFO

Received 15 September 2023 Received in Revised Form 30 August 2023 Accepted 01 September 2023 Published 25 November 2023 Available online 25 November 2023

KEYWORDS

Landsat-8 data; Aeromagnetic data; Structural mapping; Mineral exploration, Mambilla plateau,

1. INTRODUCTION

Global challenges have emerged in recent years related to access to natural resources. The ongoing rise in the economy's need for energy and minerals is being caused by expanding industrialization, and the availability of these resources is not keeping up with this demand (Abraham et al., 2019). Exploration in relatively uncharted territory is required to close the gap in natural resource availability. For the exploration and utilization of some of these essential minerals, Nigeria's Mambila plateau area offers enormous promise. When examining various resources, a variety of techniques have been used (Lyatsky, 2010; Ekwok et al., 2019). The first search for mineral and structural control occurrences must, however, mostly rely on noninvasive geophysical exploration techniques because of the relatively unexplored terrains in areas like the Mambila plateau and its surroundings. The potential field such as (aeromagnetic and pseudo gravity transform) as well as satellite imagery data.

The frequently used and aging geophysical prospecting technique known as the magnetic method of survey is The effectiveness of the technique is mostly dependent on the presence of magnetic minerals, specifically magnetite, in the subsurface rocks that support the survey area (Kearey et al., 2002; Abo-Ezz and Essa 2016; Essa and Elhussein 2017). By identifying any associated anomalies, which are typically positive and acute, it is frequently used to directly delineate the site of metalliferous ore deposits. In order to interpret these results in terms of the terrain geology, it is also utilized to decipher the spatial and directional characteristics of lineament structures, as well as the extent and configuration of magnetic source bodies (Feumoe et al., 2012).

The method works especially well in subsurface investigations of heavily dense forests where outcrops are few. In general, magnetic examinations can be carried out on land (ground magnetics), at sea (marine magnetics), or in the air (aeromagnetics). Airborne magnetics, however, become crucial to ensuring wider coverage and accessibility of remote areas of interest. The collected data show signs that represent the change in the magnetic properties of the underlying rocks, whose pattern depends on their magnetic susceptibility (Telford et al. 1990; Eyitoyo, 2016; Okpoli and Imo, 2019 and Afolabi et al., 2020; Okpoli).

Diverse anomalies with causes that can be linked to the underlying igneous or metamorphic basement are visible on a typical aeromagnetic intensity contour map. As a result, estimating depth from these anomaly signs offers helpful hints for accurately estimating the thickness of the overlying sedimentary layer. The thickness of the basement structure, in turn, sheds light on the survey area's potential for mineralization. Aeromagnetic data is used for lineament extraction to identify subsurface lineament structures that may occasionally contain economically valuable mineral ore deposits. Several augmentation and transformation methods are typically applied to the acquired aeromagnetic information in order to access the mineral potential zones of an area.

Various scholars have used aeromagnetic and remote sensing data all around the world to identify lineaments and estimate the depth of beneath basements, Connard et al. (1983), Thurston and Smith (1997), (Okpoli and Eyitoyo, 2016; Okpoli and Imo, 2019, Afolabi et al., 2020). The structural interpretation of diverse regions within the sedimentary and basement complex terrains in Nigeria has been tried by several authors (e.g., Essam et al., 2003; Anudu et al.,

2012; Okpoli and Akingboye, 2019) utilizing obtained aeromagnetic information. In most cases, several analyses such as spectra, Euler and Werner deconvolution, horizontal gradient, and Source Parameter Imaging were used to infer the depth to magnetic basement (SPI). Although there hasn't been much work done to delve deeply into research studies on the exploration and exploitation activities, the subsurface structural configuration of the Mambila plateau and its surrounding areas in northeastern Nigeria. To define the mineralized areas of commercial interest and precisely locate the ore deposits, it is necessary to connect the known mineral deposits with the known geological structures employing aeromagnetic, remote sensing, and geological structures from the geological maps. As a result, there is limited information of the area's subsurface lineaments and basement depth arrangement, and the geological structural disposition is now poorly understood.

The current research study uses a combination of exploratory data from aeromagnetic, Landsat-8 images, and pseudo gravity transforms to map anomalous zones and examine mineralization potentials in the Mambila plateau and surroundings, northeastern Nigeria. By identifying linear structures and figuring out how deep the underlying magnetic basement is, this will aid in enhancing our understanding of the structural framework in the research region.

Mineral explorers will be guided by the information learned about the structural context of the study region.

2. Study Area Location, Geological setting, and Geomorphology

The study area is located in Taraba State, Northeastern Nigeria, and is part of the Sardauna and Gashaka Local Government Areas. It comprises the southernmost tip of the eastern half of the northern region of Nigeria and is situated between latitudes 6°30' 00"N and 7°30' 00"N and longitudes 11° 00' 00 E and 11° 30' 00"E. Its total land mass is 6160km² (Tukur et al., 2005). (Figure. 1). The southern, eastern, and western portions of this plateau are locked with Cameroon (Frantz, 1981).

More than two thirds of the plateau are under the Basement Complex rocks, which range from the Precambrian to the early Paleozoic epoch (Mubi and Tukur 2005). In the meantime, volcanic rocks from the upper Cenozoic to Tertiary and Quaternary periods make up the remaining portion of the plateau and its surrounds (Jeje, 1983). The basaltic suite of volcanic rocks includes trachyte and olivine basalt. The plateau's eastern and southern escarpments are located along the Cameroonian border, while Nigeria controls the plateau's western slope and the remaining portion of its northern escarpment (Mould, 1960).

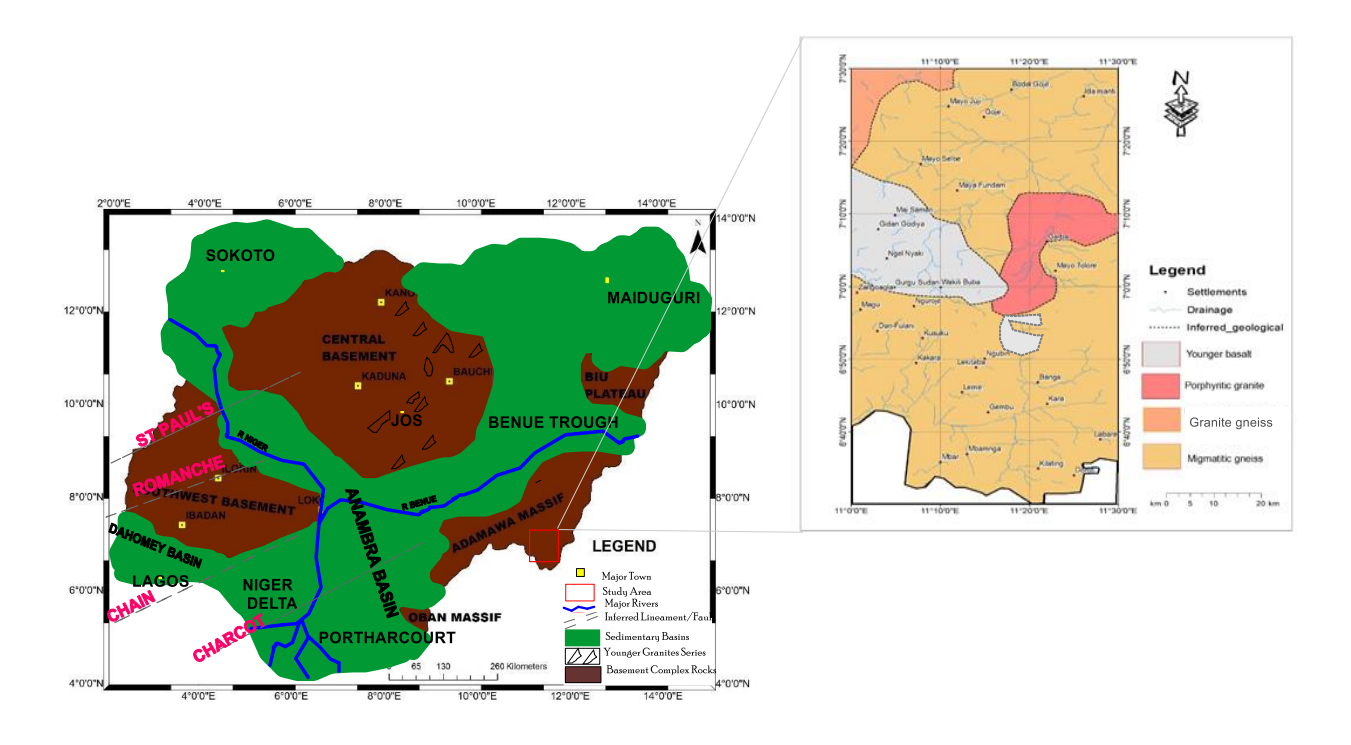


Figure 1: Structural map of Nigeria showing the three prominent fracture zones (Modified from Udensi *et al.*, 2003)

3. METHODOLOGY

3.1. Remote sensing imagery data

3.1.1. Landsat-8 image

We compared two Landsat-8 photos taken on July 7, 2020 and September 30, 2020. They contain Operational Land Imager (OLI) sensors (Roy et al., 1998). OLI offers data from nine spectral bands, with imaging resolution ranging from 15 m for the panchromatic band to 100 m infrared thermal for spectra (http://earthexplorer.usgs.gov). The spatial resolution of visible and shortwave infrared light is 30 metres. Before using the acquired data in ArcGIS 10.8.2 and ENVI 5.7, a number of preprocessing procedures were conducted, including geometric projection, atmospheric correction, spatial resolution merging, and a mosaic generation approach.

3.1.2. Band ratio (BR)

Differentiating rock units and understanding hydrothermal alteration zones requires the use of the Band Ratio (BR) method, which is based on differences in the spectral signature of minerals and various rock units (Goetz et al., 1983). Because different alteration minerals absorb light at different wavelengths, a BR technique is often necessary in mineral or lithological mapping to enhance spectral sensitivity within alteration zones (Pour et al., 2019). Because of this, an RGB composite image can be utilised to accurately discriminate between OH-bearing minerals and iron oxides by selecting the appropriate ratios in the BR method.

3.1.3. Constrained energy minimization (CEM)

On each and every signal, the Constrained Energy Minimization (CEM) algorithm was applied (Farrand and Harsanyi, 1997, Harsanyi, 1993). The relevance of CEM has grown over time, and it is now one of the strategies that is utilised the most frequently in the process of mapping the abundance of targets. By considering all features other than the target as the unknown background, this method maximises the reaction of the target spectrum while minimising the reactions of all other features. This is accomplished by treating all features as though they were the unknown background. It is beneficial in the process of identifying alteration zones based on the spectral signatures of the minerals that cause the alteration. The spectral fingerprints of the minerals were obtained from the USGS spectral collection and analysed using ENVI V.5.3.

3.1.4. SRTM DEM data

The international Shuttle Radar Topography Mission (SRTM) project creates a Digital Elevation Models (DEM), which is short for "Digital Elevation Models," which is a complete digital topographic database of Earth with a high resolution (Nikolakopoulos et al., 2006). According to Suzen and Toprak (1998), it is possible to automatically derive surface lineaments using DEM data. Automatic lineaments mapping using shaded SRTM DEM 90m data was used in order to build shaded relief pictures, which are beneficial for the extraction of surficial lineaments and faults. These pictures can be helpful in the process (Ganas et al., 2005). Lines are automatically extracted from the shaded relief photographs using (PCI Geomatica 2015) using the default parameters. After that, the output is manually edited to omit any manmade features (buildings, roads, etc.) in order to

improve the agreement between the extracted lines and the geological properties. This is done in order to maximise the potential of the extracted lines.

3.2. Aeromagnetic data

Nigerian Geological Survey Agency (NGSA) magnetic data grids for sheets 276 (Gashaka) and 295 (Mambilla) were processed using Geosoft Oasis Montaj TM 8.4.2. Aeromagnetic information was gathered with the help of a Scintrex CS3 Cesium Vapour magnetometer, which samples at 0.1 s and can measure changes in Total Magnetic Intensity (TMI) to within 0.001 nT. The data was collected at an altitude of 5000 metres with a tie line interval of 500 metres. The collected aeromagnetic data were preprocessed before being reduced to a format that has a clear and direct relationship with subsurface geology. The magnetic data from the combined map of Gashaka (sheet 276) and Mambilla (sheet 295) were improved using techniques like reduction to magnetic equator (RTE), regional/residual field matched filtering, first and second vertical derivatives, total horizontal derivative, analytical signal, and pseudo-gravity transform, as well as MAGMAP's step-by-step filtering processing (Okpoli and Eyitoyo, 2016).

3.2.1. Reduction to the equator (RTE)

There are two parts to Reduction To the Equator (RTE): the phase (Icos(I) $\cos(D-\delta)$) and the amplitude ($\sin(I)$ term). The numerical inaccuracy (from the term of 0/0) in the amplitude adjustment (the $\sin(I)$ component) done when (D- δ) is /2 can cause North-South features to burst when travelling to the equator from low latitudes (i.e., a magnetic east-west wave number). To reduce or eliminate this problem, it is possible to slightly undercorrect the

amplitudes of close North-South features, which are expressed as follows in the Geosoft Oasis Montaj software.

$$L(\theta) = \frac{[\sin(1) - i.\cos(1)\cos(D - \theta)]^2 x(-\cos^2)(D - \theta)}{[\sin^2(Ia) + \cos^2(Ia).\cos^2(D - \theta)] x[\sin^2(I) + \cos^2(I).\cos^2(D - \theta)]}$$
(1)

if (|Ia| < |I|), Ia = I

where I is the geomagnetic inclination, I α is the amplitude correction inclination, and D is the geomagnetic declination.

3.2.2. Upward Continuation

It is effective for regional-residual separation because upward continuation attenuates the anomalies of shallow features while amplifying the anomalies of deeper sources. The residual field consists of the shallow features remaining after subtracting the relatively deeper sources from the total field (Tanaka et al., 1999). The frequency response of the upward continuation filter is represented as follows:

$$F_u(u, v, h) = e^{-2\pi h} (u^2 + v^2)^{1/2}$$
(2)

where "u" and "v" are the frequency-domain equivalents of the x and y axes, and "h" is the vertical extent of the field. Using upward continuation helps reduce the impact of tiny surface characteristics (Telford et al., 1990). Attenuation of topographic impacts is another use. For the whole F-category (x, y, 0).

$$F(x, y - h) = \frac{h}{2\pi} \iint \frac{F(x, y, 0) \delta x \delta y}{(x - x')^2 + (y - y')^2 + h^2}$$
(3)

By using the surface values of magnetization and the upward continuation equation (Equation 3), we may determine the magnetization of any point in free space. Total field at point P(x, y, -h) above the known surface F(x, y, 0) is shown on the left (Telford et al., 1990).

3.2.3 Edge detection and depth to basement estimation techniques

Multiple Fourier-based methods are utilised during inversion, including spectral and 3D interface-based inversion (Spector & Grant, 1970) and optimization (voxel) techniques (Salem et al., 2007; Werner, 1953). These methods invert potential field data to determine the 2D or 3D subsurface susceptibility distribution, which

specifies the origin of magnetic anomalies. All of these inversion methods are used in this investigation with the exception of the voxelbased method. Below, we offer the governing equations that characterise each method.

3.2.4 Analytic signal (total gradient)

The total gradient approach can be used to precisely find horizontal structures in the Earth's crust (such as contacts, intrusions, faults, and sheet sources), notwithstanding the magnetic latitude. These horizontal structures include contacts, intrusions, and faults (Phillips, 2000; Azizi et al., 2015). In most cases, the magnetic direction of the source does not impact the analytical signal. Because of this, the analytical

signal is largest in the middle of the magnetic structure and has smaller peaks near the magnetic structure's extremes (Nabighian, 1972). For the interpretation of aeromagnetic data collected close to the magnetic equator, the absence of magnetization direction in the shape

of the overall gradient amplitude is desirable (MacLeod et al., 1993). After adding together, the gradients of the magnetic anomaly in three orthogonal directions, one arrives at the total gradient (Roest et al., 1992).

Total gradient
$$(x, y, z) = \sqrt{\left(\frac{\delta M}{\delta x}\right)^2 + \left(\frac{\delta M}{\delta y}\right)^2 + \left(\frac{\delta M}{\delta z}\right)^2}$$
 (8)

Aeromagnetic anomaly data from the research area was analysed and mapped using the total gradient filter, where TG (x, y) is the total gradient of the aeromagnetic anomaly field.

3.2.4 Total horizontal derivative of tilt angle

Spectra generated by tilt filters include the complete horizontal component of the tilt angle derivative (THDR-TDR). The hypothesis that zero contours represent the edges of the creation of equations is used to increase weak and strong magnetic anomalies over the researched area. Additionally, this hypothesis is used to determine the structures, trends, lithologic contact, edges, and boundaries of magnetic sources, particularly at shallow depths (2 and 3).

$$D = -\frac{1}{K_{\text{Max}}} = \frac{1}{\sqrt{\left(\frac{\delta Tilt}{\delta x}\right)^2 + \left(\frac{\delta Tilt}{\delta y}\right)^2}}$$

THDR_TDR=
$$\arctan^{-1}(\frac{1\text{VD}}{\text{HD}_{TDR}})$$

Here, 1VD represents the first vertical derivative in the z-axis, dT/dx represents the derivative in the x-axis, and dT/dy represents the derivative in the y-axis.

3.2.5 Spectral analysis

By converting the digitalized gravity/magnetic data from space domain to frequency domain, power spectrum analysis is used to potential field anomalies in a single dimension. According to an enhancement by Kebede et al. (2020), the transformation is applied to calculate the power or amplitude spectrum as:

$$f_{\omega} = \sum_{K=0}^{N-1} f(\mathbf{k}) e^{-t\frac{2\pi nK}{N}}$$

The spectrum of discrete amplitudes, denoted by F ω , can be expressed as the product of real and imaginary parts.

$$F(\omega) = a(\omega) + ib(\omega)$$

And with $\omega = 2\pi f$; f being the linear frequency and ω the angular frequency. The amplitude of /F (ω)/ is expressed as:

$$/F(\omega)/ = \sqrt{a^2\omega + b^2}\omega$$

The spectrum shows how the energy changes with different wavelengths and frequencies (Likkason, 2013).

$$h = -\frac{1}{4\pi} \left(\frac{\log g_1 - \log g_2}{K_1 - K_2} \right)$$

This technique uses low and high frequency anomalous bodies to generate a statistical estimate (Spector & Grant, 1970). These irregularities can be broken down into three distinct categories based on their typical frequencies: low, middle, and high (Kebede et al., 2020). In this study, we use power spectral analysis to invert the profile data along the rift axis ((Figure 4), white line) to determine the depths of the sources at the several basement interfaces. Equation can be used to get the depths at any point along the line. Several researchers used this method (Mammo, 2012) to estimate basement interface depths from profile data, and the analysis outcomes (depths of susceptibility contrasts) are addressed in greater detail here.

3.2.6 Source parameter imagery (SPI)

This technique uses low and high frequency anomalous bodies to generate a statistical estimate (Spector & Grant, 1970). These irregularities can be broken down into three distinct categories based on their typical frequencies: low, middle, and high (Kebede et al., 2020). In this study, we use power spectral analysis to invert the profile data along the rift axis ((Figure 4), white line) to determine the depths of the sources at the several basement interfaces. Equation can be used to get the depths at any point along the line. Several researchers used this method (Mammo, 2012) to estimate basement interface depths from profile data, and the analysis outcomes (depths of susceptibility contrasts) are addressed in greater detail here.

$$A(x,z) = \frac{\partial B(x,z)}{\partial x} - j \frac{\partial B(x,z)}{\partial z} \text{ or } A(x,z) = /A/\exp(j\theta)$$

Where, $/A/ = \sqrt{\left(\frac{\partial B}{\delta x}\right)^2 + \left(\frac{\partial B}{\delta y}\right)^2}$ is analytical signal amplitude. According to Thurston and Smith (1997), equation (1) can also be represented as the local frequency 'f', provided by equation (9).

$$f = \frac{1}{2\pi} \frac{\partial}{\partial x} tan^{-} \begin{bmatrix} \frac{\partial B}{\partial z} \\ \frac{\partial B}{\partial x} \end{bmatrix}$$

Often more convenient to re-advance as:

$$K = 2\pi f = \frac{1}{A^{2}} \left(\frac{\partial^{2} B}{\partial x \partial z} \frac{\partial B}{\partial x} - \frac{\partial^{2} B}{\partial x^{2}} \frac{\partial B}{\partial z} \right)$$

Thus:

$$h = \frac{1}{K_{\text{Max}}}$$

The work is started by calculating the grids as $\left(\frac{\partial B}{\partial x}, \frac{\partial B}{\partial z}\right)$ and $\frac{\partial B}{\partial y}$. The 2-dimensional slope contact model that SPI uses predicts that the highest K values will be found above the sloping contact. For magnetic sources, the depth values are estimated by substituting equation (2) into the following expression in Eq. (3):

$$Depth = \frac{1}{K_{\text{Max}}}$$

Where the maximum value of K above a sloping 2-D contact is represented by Kmax in equation (12). (equation 11). Aeromagnetic data from the Niger-Benue River confluence zone and its environs were analysed using the local wavenumber approach to calculate the depth values of sources inside the basin and its environs. This is done so that the sedimentary layer depth of the basin and the depth range values of the sources inside the nearby basement terrain may be calculated.

3.2.7. Pseudo-gravity data analysis

Because gravity anomalies are more instructive and simpler to understand and measure than magnetic anomalies, pseudo-gravity transformation is helpful in the interpretation of magnetic anomalies. This is not because a mass distribution matches the magnetic distribution beneath the magnetic source (Blakely, 1995). The applied pseudo-gravity transform to magnetic data was originally done by Baranov (1957). This technique made it easy to eliminate the distortion brought on by the earth's magnetic field by shifting the magnetic anomalies' apex over the source body. Transformation techniques were used on the data to identify and delineate crustal magnetic sources, since magnetic anomalies are rarely centred above their origins. With Oasis Montaj version 7.0.1, the Fast Fourier Transform (FFT) filter extension was utilised to apply the pseudo-gravity transform on the residual of the total magnetic intensity data.

A magnetic anomaly that was a dipole before undergoing pseudo-gravity transition will become a monopole and appear to be a gravitational anomaly once the transformation is complete (Subarsyah and Priohandono, 2016). Because the outputs of this transformation are comparable to gravity data from a magnetic object when the density ratio is taken into account, it is utilised in the interpretation of magnetic anomalies. This translation states that one ampere per metre is equal to 102 gamma, and one gamma is equal to one kilogramme per cubic metre. According to Blakely, the proportionality should be understood to be 100 kg/m3 for every metre (1995).

For a magnetized body, the magnetic potential V due to proportional density, and the gravitational potential, U can be related by the following Poisson' relation:

$$V = -\frac{c_m}{\gamma \rho} M \hat{m} \xrightarrow{\nabla} p_U \tag{9}$$

$$=\frac{-c_m M g_m}{\gamma \rho} \tag{10}$$

Where V represents magnetic potential, U represents gravitational potential, gm represents the component of gravity in the direction of magnetization, represents Newton's constant, represents rock density (g/cm3), Cm represents magnetic constant, and is magnetization (Am-1). Assuming that M and are constants for this transformation, the Fourier transform equation is (2016) Subarsyah and Priohandono.

$$F[g_m] = \frac{\gamma}{C_m} \frac{\rho}{M} F[V] \tag{11}$$

Where,

$$F[V] = -\frac{1}{\theta_f|k|} F[\Delta T] \tag{12}$$

So that,

$$F[g_m] = -\frac{\gamma}{c_m \theta_f |\mathbf{k}|} \frac{\rho}{M} F[\Delta T]$$
 (13)

$$F(psg) = -\frac{\gamma}{c_m \theta_f |\mathbf{k}|} \frac{\rho}{M} \tag{14}$$

 g_m in this case is pseudo-gravity.

RESULTS AND DISCUSSION

4.1 Surface structural trend analysis of lineaments

The remaining uncorrelated bands are blended into RGB, and the False Colour Composite (FCC) of bands 753 and 764 (Fig. 2) developed models based on their correlation coefficient. The lithologies and alteration zones were mapped

using these two colour composite models (Figure 2), which were created from Landsat-8 Mambilla and its surroundings. The textural characteristics of the outcrops allow them to be identified in the photograph from the background. The crystalline texture and structural features of the rocks in the image's area segment are clearly seen in the bands' natural RGB colour combination.

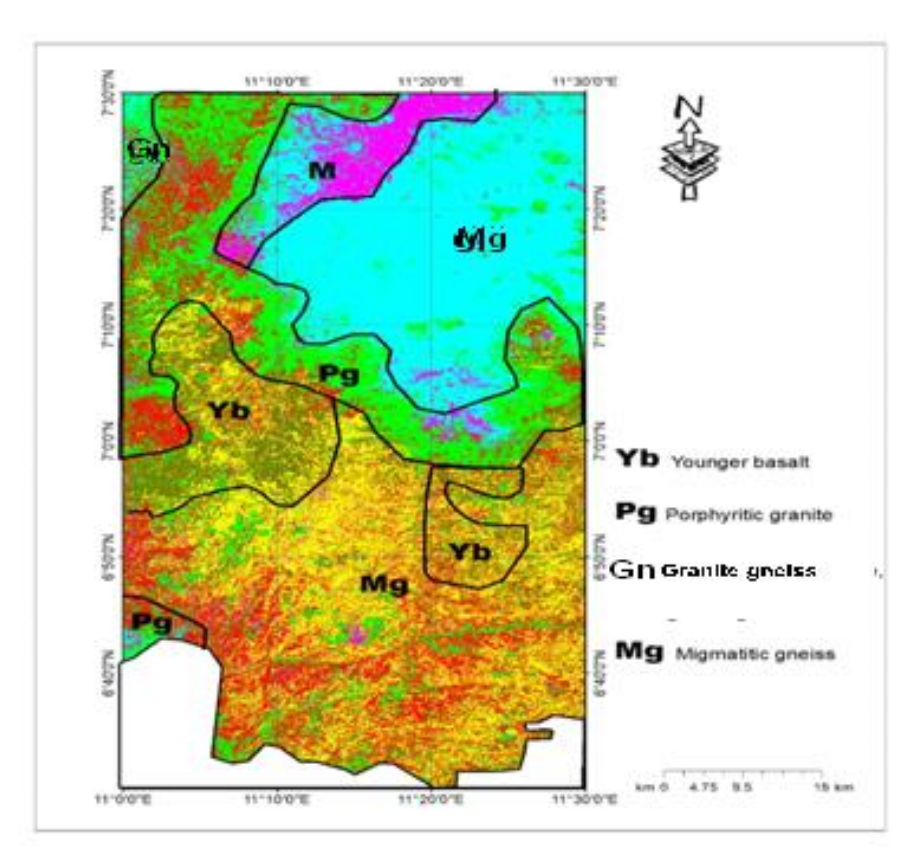


Figure 2: Landsat-8 ETM+ false color composite image (bands 7, 4, 2 in R, G, B) younger basalt (yb), porphyritic granite (pg), granite gneisses (Gn) and migmatite gneiss (Mg).

4.1.2. Principal Component analysis (PCA)

The PCA normalises the seven OLI bands and strengthens, compresses, and limits the leading bands. Each one was linearly improved to produce composite images (El-said et al., 2014). Bands 2456 and 716 were the PCAs employed in this investigation (Figure 3). Figure 3 displays the results of the statistical calculations in the form of individual photos and varied percentages of the collected data. Because of the high reflectance in band 6 (0.451293) and low absorption in band 3, the pixels in PC2 of PCA 2456 are quite luminous (-0.434848), the eigenvectors showed that the majority of the younger basalt, porphyritic granite, granite gneisses, and migmatite-gneisses could be distinguished from one another. On the other hand, dark pixels were indicative of migmatite, and granite gneiss. The aforementioned rocks were also recognised as bright green, purple, yellowish, and pinkish pixels in the RGB composite of PCA 716 (Figure 3).

Despite the fact that the positive absorption eigenvector in band 6 (0.518572) and the negative in band 4 (-0.959506) mapped dark pixels, PC2 was used to differentiate between the PC of 2456 of the younger basalt, porphyritic granite, and migmatite gneisses. This followed the positive eigenvector value in band 4 and the negative eigenvector value in band 5. The PCA 716 image composite shows that the reddish and pinkish pixels are associated with the migmatite gneisses rocks in the study area. There was a strong relationship between the various rock types in the study region and the geological map of Mambilla and the surrounding area.

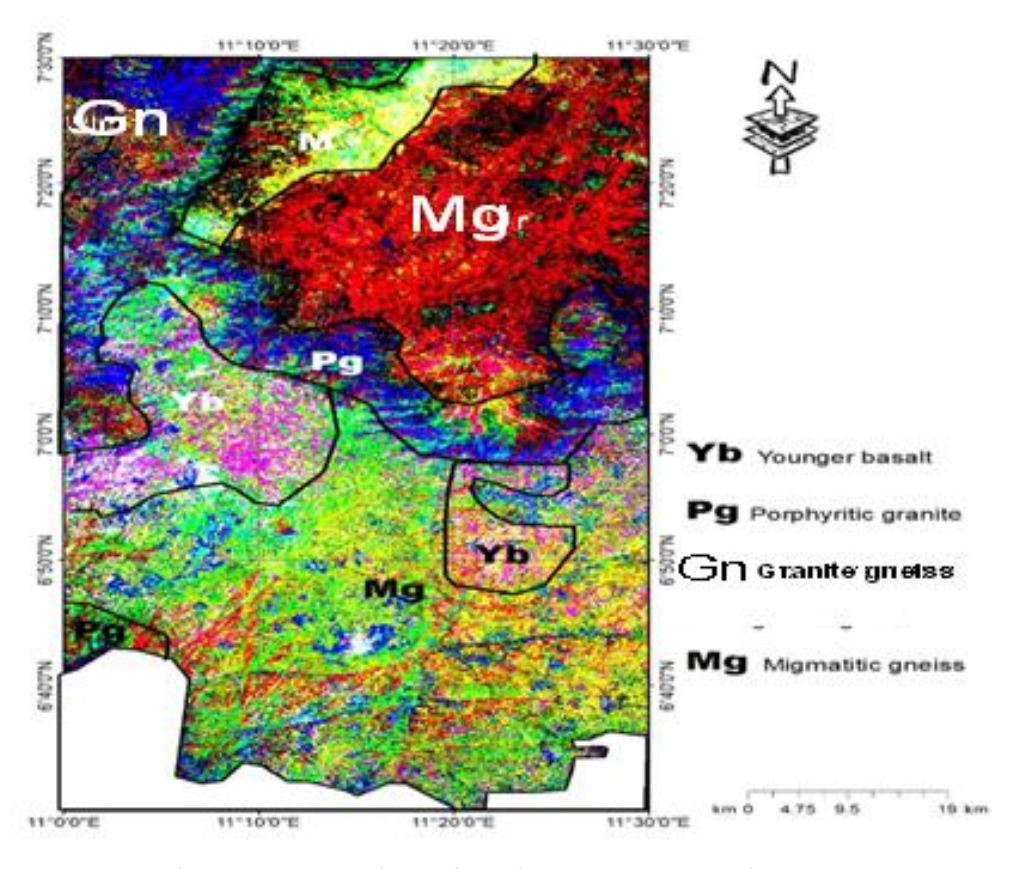


Figure 3: Principal component analysis of Landsat 8 ETM+ image (PC2, PC1, PC4 in R, G, B) of the study area. Younger basalt (Yb), porphyritic granite (Pg), granite gneisses (Gn) and migmatite gneisses (Mg)

4.1.3 Lineament Trend Analysis and Structural Density Map of the Area

From satellite and aeromagnetic data, the surface lineaments (Figure.7 and 8) are automatically derived, representing zones of structural density. Because of their structural control, mining sites have a high structural density, highlighting the significance of the lineaments density map in the identification of prospective mineralization zones (Abdelnasser and Kumral, 2017). Using the lineament detection from the magnetic (CET grid approach) and satellite data(Figure 7), a structural and lineament map was created from aeromagnetic, satellite (Figure 8) and magnetic data(Figure 7). Aeromagnetic and satellite data show a rose diagram with zones of high structural complexity,

with a main NE-SW trend and less common NNW, WNW, NS, and NE trends (Figure 9 and 10). These tendencies are positively correlated with the tendencies of zones of recognised minerals' structural complexity near the surface. Mined in places like Maisamari, Gurgu, Yelwa, Mayo Ndaga, Lekitaba, and Nguroje, these solid minerals include, among others, blue sapphire, aquamarine, tourmaline, amethyst, cassiterite, and bauxite. In order to verify the efficacy of the methods employed. The results of the present investigation show striking similarities to other published field geoscientific data in terms of their primary tendencies. While (Klemm and Klemm, 2013) recorded the northwesterly direction as a major trend for mineralizing Gold, (Abdelnasser and Kumral, 2017) found that mineralization in

the Maisamari, Gurgu, Yelwa, Mayo Ndaga, Lekitaba, and Nguroje areas follows brittle-ductile shear zones of NE-SW direction, in addition to other structures with NE-SW and E-W directions. Gold mineralization is linked to NW-SE and N-S trending structural characteristics (such as faults and shear zones), as noted by El-Desokyet al., (2021). According to Helmy et al. (2004), the most common orientations for gold-quartz veins are N, S, NNE, and SSW, with the occasional occurrence of NW-trending, non-mineralized quartz veins. According to Klemm &

Klemm (2013), the primary quartz lodes strike northeast to southwest, whereas the mined quartz veins follow a shear zone from northwest to southeast and east to southwest. To further identify the structural density zone, a map of lineaments was derived from the Digital Elevation Model (Figure 12) (see Figure 11). There is a positive relationship between higher lineament density and sites' of mineralization, and Fig. 11 shows that the locations where mining is now taking place have medium to high lineament density.

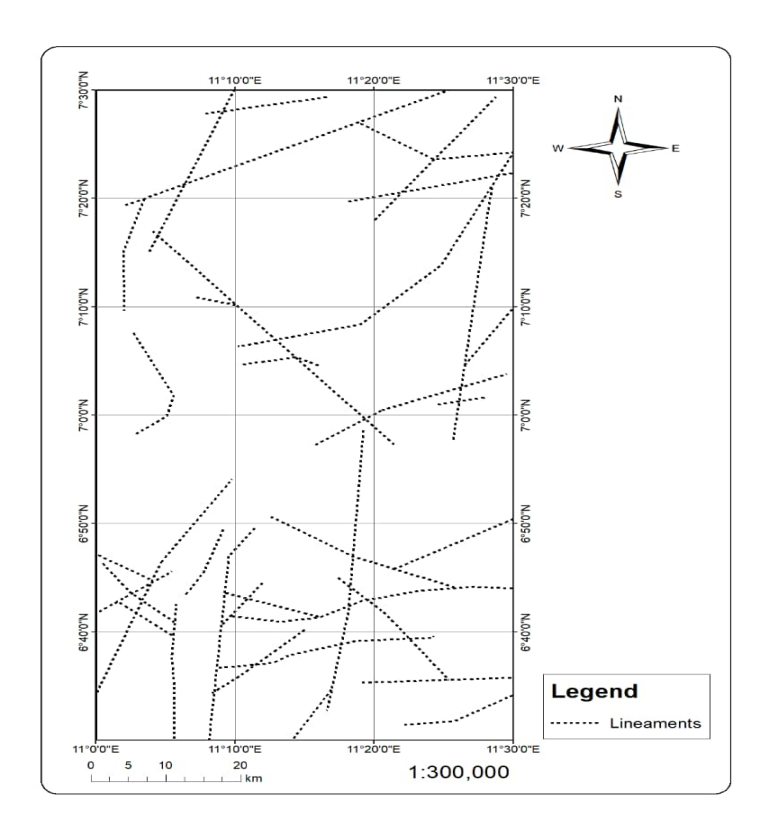


Figure 7: Structural lineaments map of the study area extracted from satellite data

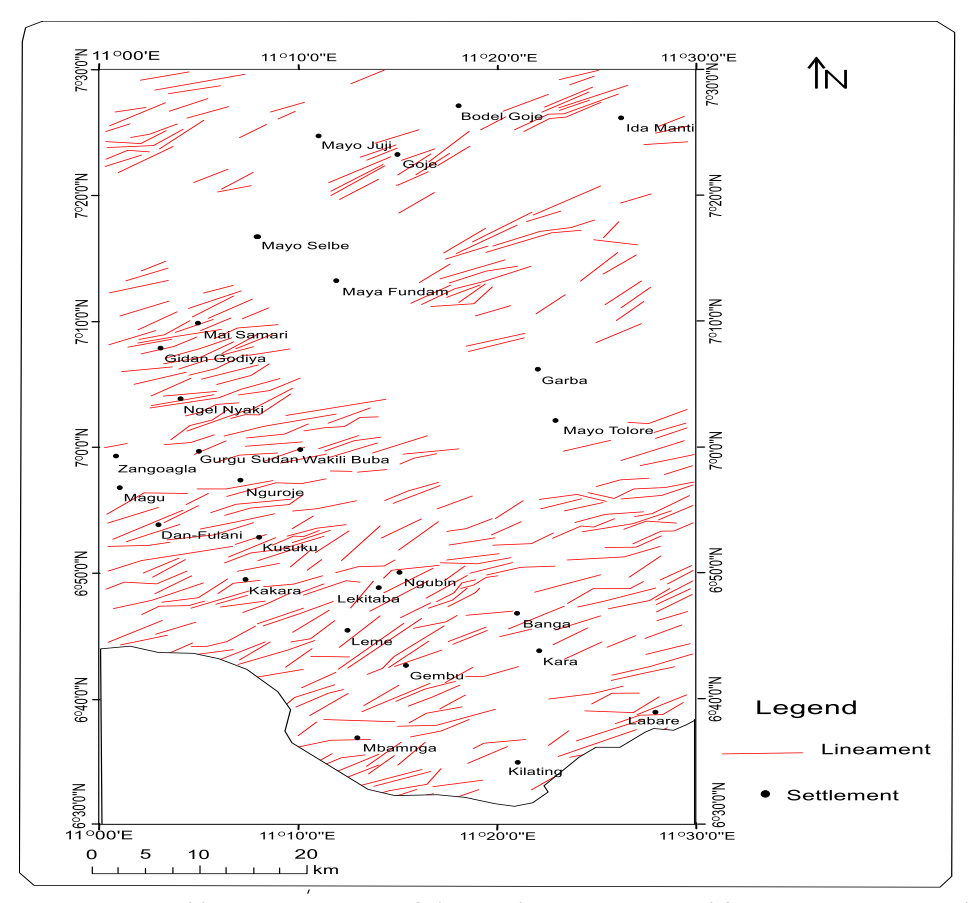


Figure 8: Structural lineaments map of the study area extracted from aeromagnetic data

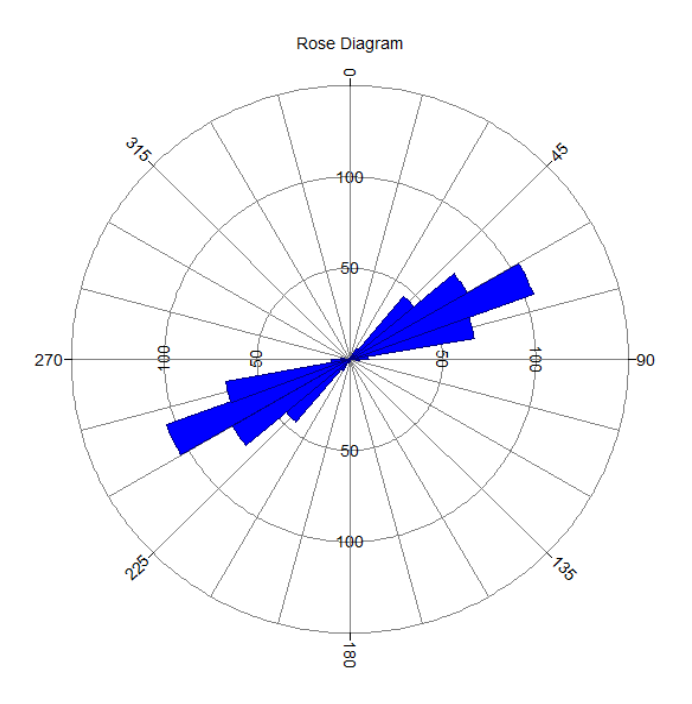
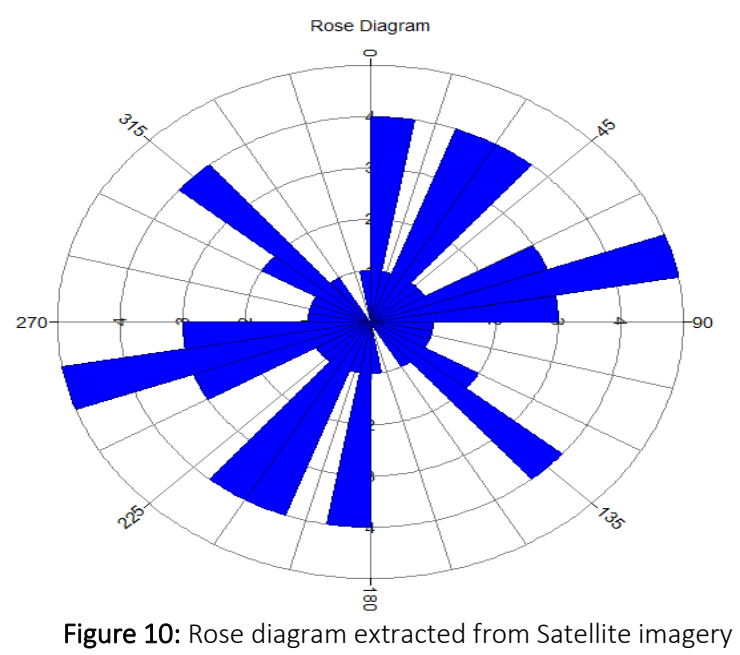


Figure 9: Rose diagram extracted from aeromagnetic data



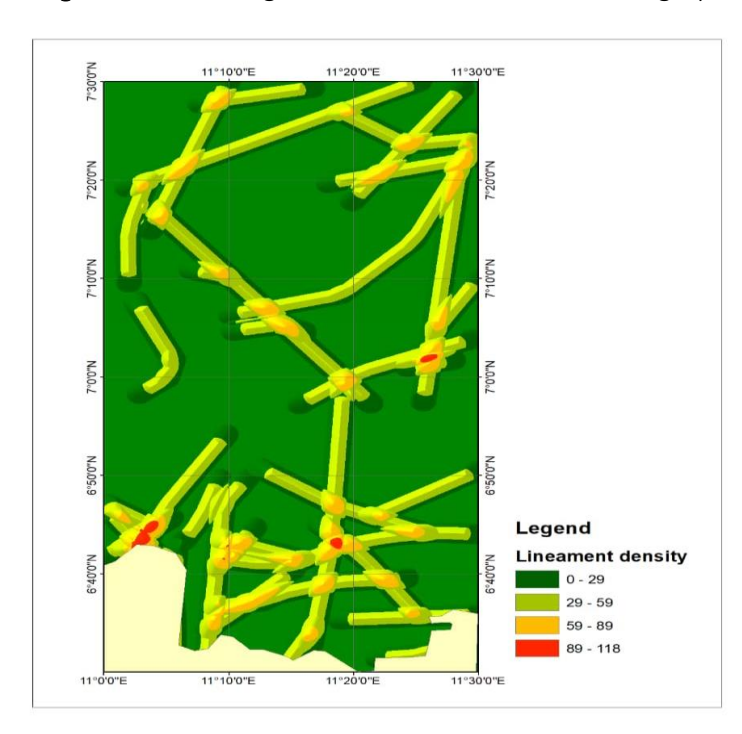


Figure 11: Lineament density map of the study area

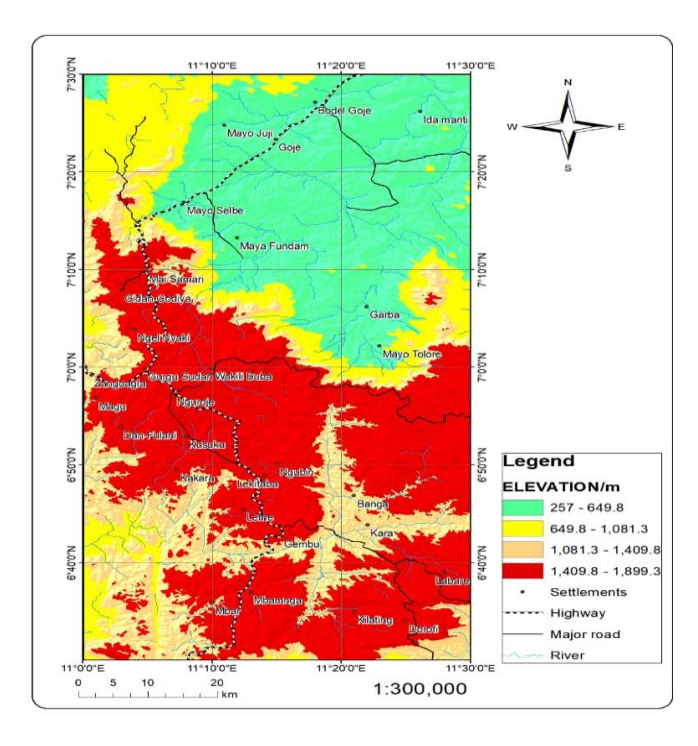


Figure 12: Digital elevation map of the study area

4.2. Aeromagnetic data analysis

4.2.1. Total magnetic intensity (TMI), Crustal field and Reduction to equator (RTE)

Fugro gathered and stored the data in the following manner: X columns stand for longitude/easting, Υ columns for latitude/northing, and Z columns for total magnetic intensity (TMI). In order to simplify processing, the aeromagnetic total field intensity value (Z) of 33,000 nT was removed. In order to obtain the Z-column total, a simple arithmetic addition of 33,000 nT to each value of the Z column had to be done after obtaining the data from NGSA before any further processing could be deemed legitimate. Once the Universal Transverse Mercator (UTM) projection method was used for georeferencing, X and Y were determined to be the ideal columns. The data gridding process ultimately produced the grid that represented the aeromagnetic total field strength in terms of colour images. The colorcoded aeromagnetic total field intensity of the

study area is shown in (Figure 4). The asymmetrical and low-data values associated with the structural features' NE-SW patterns and linear relationship to the southern half of the map are used to categorise them. With a deviation from mean of 31.50 and a mean of 33068.89nT, the lowest and maximum values for the gridded data were 33030.343nT and 33172.792nT, respectively. Over the region, the inclination calculated geomagnetic declination range from -0.3° to 7.2° (mean: 3.5°) and -2.5° to -1.5° (mean: 0.24°), respectively. The study location is clearly located in a low magnetic latitude region. research The southernmost section exhibited near-surface igneous rock possessing elevated magnetic susceptibility and magnetic intensity values.

The Total Magnetic Intensity (TMI) map over Mambilla and its surroundings displays an average value of 33078.888 nT, with TMI values ranging from 32892.772 nT to 33203.596 nT (Fig. 4). High, low, and intermediate magnetic signals

that can be attributed to rock susceptibility, depth to the source of magnetic rock, degree of strike, and remnant magnetism make up the resulting TMI map (Likkason, 2014). Among the villages with the highest TMI values were Gidan Garba, Maisamari, Gidan Godiya, Nguroje, Ngubio, Banga, Kakera, and Kilating. MajoTolore,

NgelNyeki, Kuuku, Dan Fulani, Magu, Gidan Godiya, Mayo Juji, Bode Goje, Ida Manti, Mayo Selbe, Mayo Fundam, and Kara are among the areas where the Northeast-Southwest trends (Fig. 4) are evident. These trends are the dominant trend and lineaments observable in the study area.

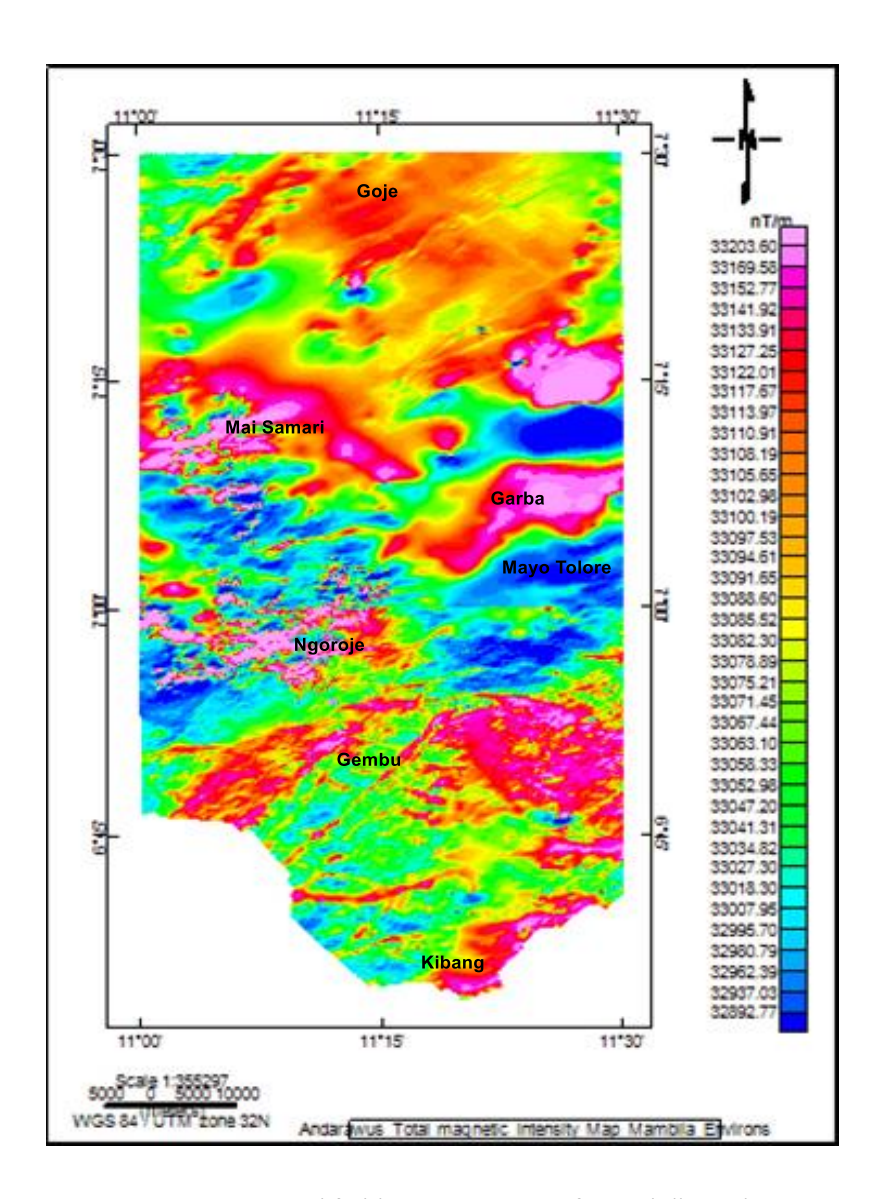


Figure 4: Aeromagnetic total field intensity map of Mambilla and environs

The values on the Main Magnetic field map over Mambilla and its surroundings range from 33228.522 nT to 33358.377 nT, with an average of 33293.4495 nT (Figure 5). This field is a representation of the research area's regional field that isn't on the (TMI) map. The villages Kilating, Kara, Leme, Dan Fulani, Mbanga, and Gembu, which trend NW-SE (Figure 5) and gradually grow from SW-NE, were found to have the lowest main fields.In addition, the main field

rises from Ida Marti to Bode Goje; the highest main field was noted in the research area's far northeast. The NW-SW trend is the primary pattern for the entire main field (Figure.5).

The magnetic field of the crust was determined by deducting the measured magnetic field from the estimated magnetic field (Thompson, 1982). The 2005 DGRF model served as the basis for the magnetic field correction in this specific investigation.

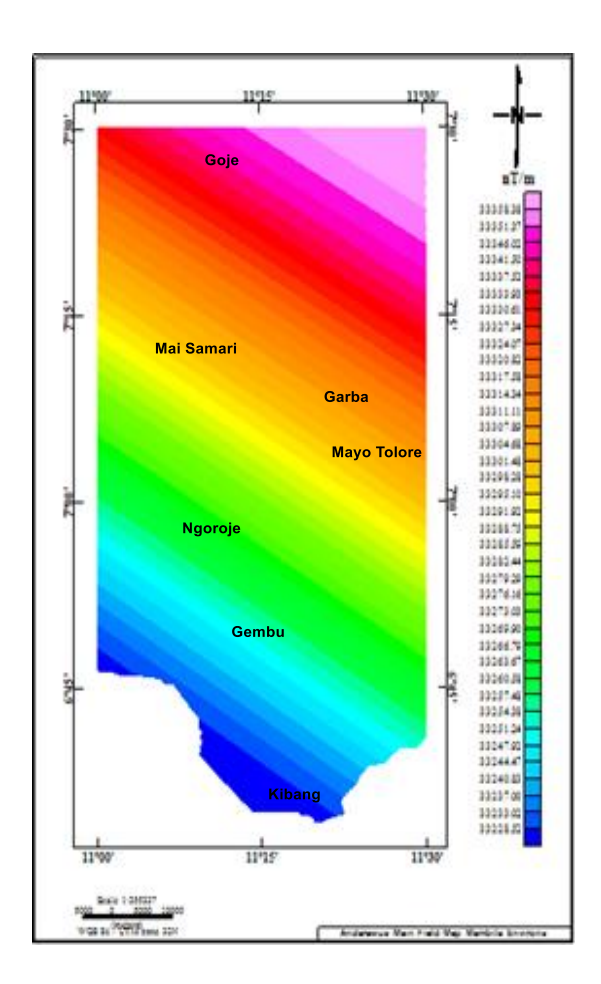


Figure 5: Map of Generated Geomagnetic main field of Mambilla and environs

The average value of the crustal magnetic field map over Mambilla and its surroundings is - 159.50nT, with values ranging from -397.669nT to -80.699nT (Figure 6). Pyroxene, olivine, magnetite, ilmenite, plagioclase feldspar, and

other minerals are among the many minerals found in basaltic rocks (Auckland 2005). The high interval of the local magnetic anomaly value is thought to have been largely caused by the magnetite found in basaltic rocks. Differences in

the geological, magnetic, and chemical compositions of the rock masses are indicated by variations in the crustal magnetic field within the study area. Whereas the pink-colored portions indicate strong magnetization, the blue-colored areas indicate low magnetization. As seen in Figure 6, areas with high magnetic values (pink colour) have magnetised entities that are shallow to near the surface. The migmatite-gneiss complexes are most likely exposed on the surface or may have been buried at relatively shallow depths, as indicated by the high magnetic anomalies found in the majority of the studied area. Conversely, regions with low magnetic

values (blue hue) are caused by magnetic basement subsidence brought on by the epeirogenic uplift within the research area as well as deep-seated magnetised substances. As seen in (Figure.6), the values displayed by the study area's crustal field map are all negative, indicating a magnetic equatorial zone. The earth crustal field anomaly combines the unique impacts of mutually more extensive and deeper sources that are identified as local and regional sources and are regarded as noise. Consequently, residual anomalies are the anomalies of interest (Likkason, 2014).

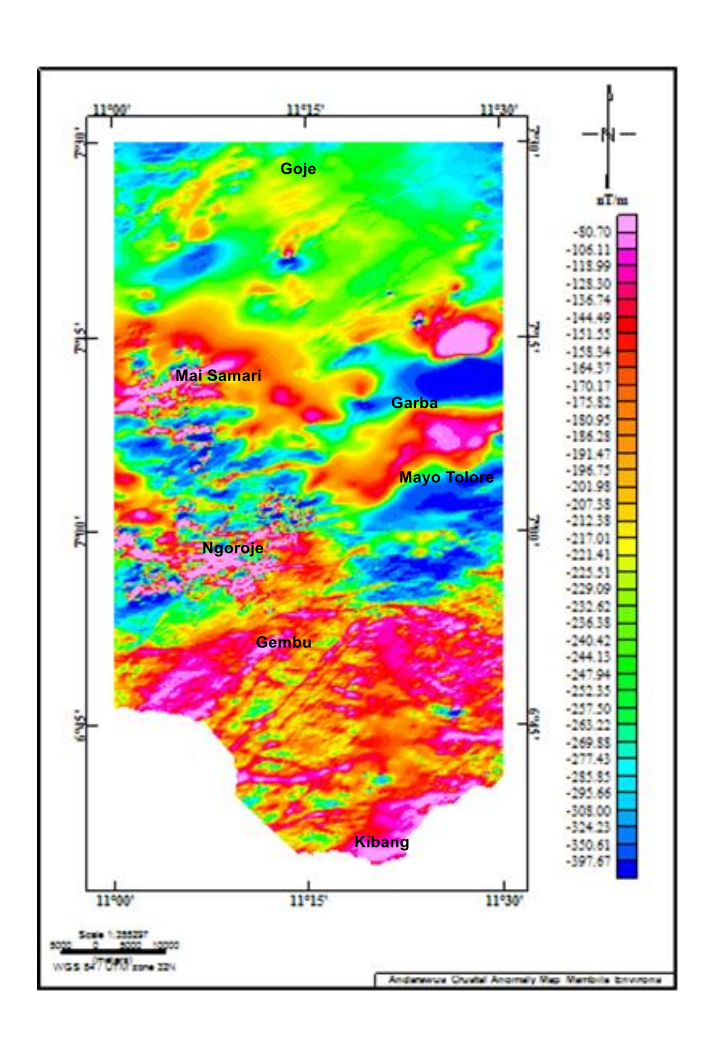


Figure 6: Crustal field (TMI) anomaly map of the study area

The RTE map aids in removing the magnetic inclination effect in the low magnetic latitude zone by aligning the magnetic anomalies of the peaks with their sources and enhancing the basement architecture to include structural lineaments with their orientations. The magnetic strength variation over the research area led to identifying two primary magnetic zones. Strong magnetic anomalies with amplitudes ranging from -82.382nT to -119.153nT predominate in

the western, central, southern, and eastern regions (Figure.7). Nonetheless, the area's northern, northwest, and extreme southern regions are distinguished by relatively low amplitude magnetic intensity values (between -130.00nT and -392.122nT), which are indicated by greenish to blue colours and suggest regions with low magnetic content in their geological structures (fractures/faults).

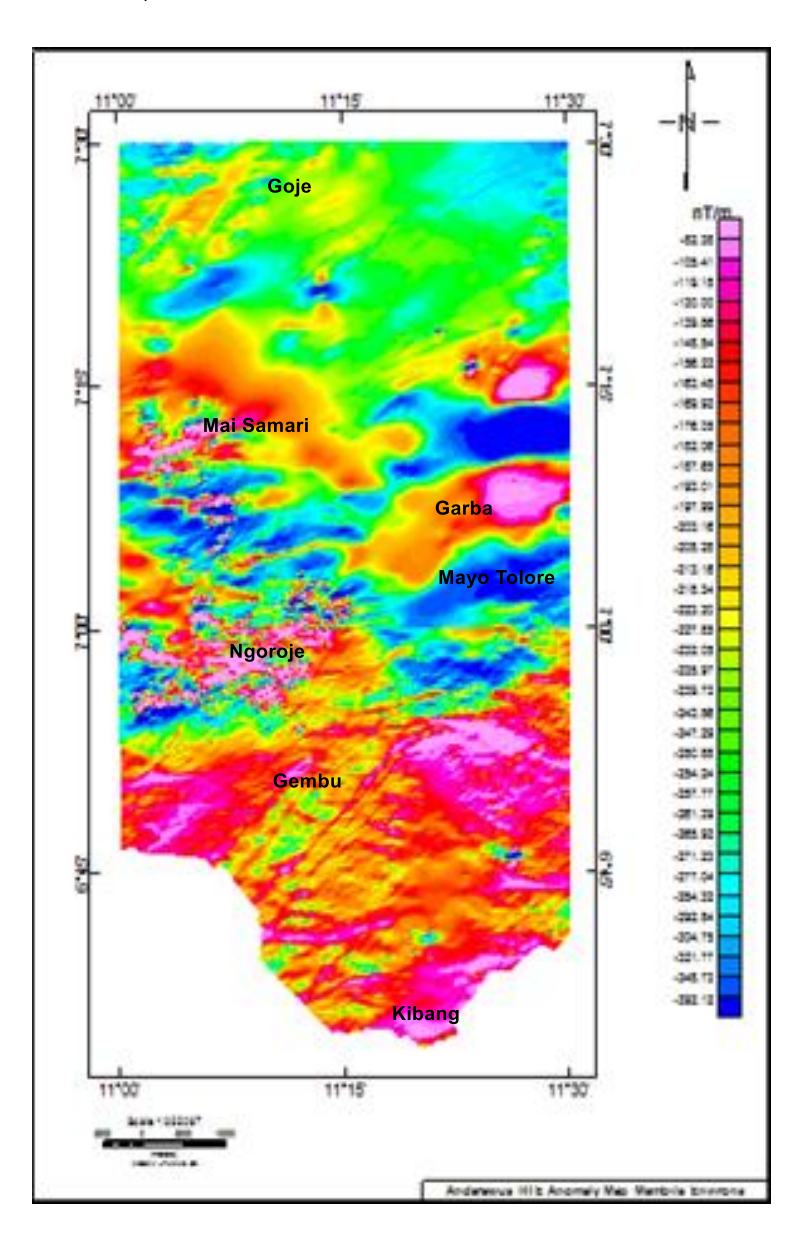


Figure 7: Reduction to equator map of Mambilla and Environs

4.3.3. Upward continuation

Over Mambilla and its surroundings, the reduction to a magnetic equator field map was upward continued for 15 km, displaying values ranging from -279.141 nT to -157.160 nT. Compared to the crustal magnetic field in Figure 6, these upward continuing field levels are smaller. The areas of Mbanga, Gembu, and Kilating exhibit the strongest magnetic field, trending NW-SE (Figure 8). The magnetic field gradually decreases from SW-NE through May Tolore, followed by Bode Tolere, which likewise

exhibits a NW-SE pattern. The NW-SE trend is the primary trend of the entire upward-trending field (Figure 8). The data on anomalies has been continuously collected upward until the anomaly contour pattern exhibits a generally steady or non-changing pattern (Ilapadila et.al. 2019). The magnetic anomaly contour map exhibits a smooth pattern at a height of 15 km, according to the analysis result of the anomalous contour pattern after upward continuation. Figure 8 displays the magnetic anomalous patterns that are the visual outcome of the upward continuation process starting at a height of 15 km.

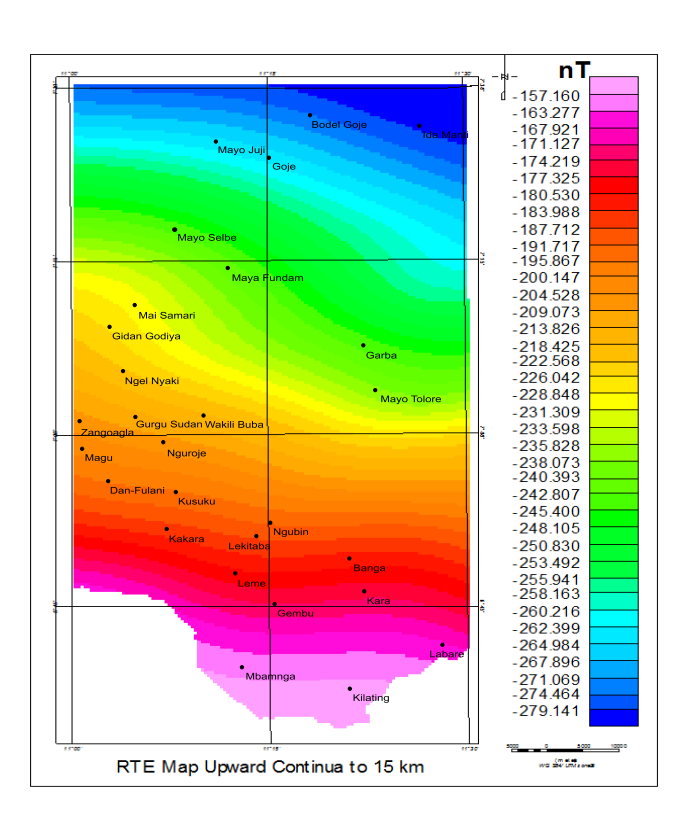


Figure 8: Upward Continuation ma at 15km of Mambilla and environs

4.3.4. Analytic Signal (total gradient)

Figure 9 displays the estimated depth to magnetic sources, which falls within the range of 0.348 km to 2.55 km. The maximum for the magnetised body is shown in the centre of each circle in Figure 9, and the estimated depth of the

source is shown as a function of the circle's diameter. The Analytic Signal approach avoids the problem of dislodged contacts since it does not rely on the same simplifying assumptions as the Horizontal Gradient Magnitude method. Analytic Signal contacts, on the other hand, are

not as steady, and their trajectories may be skewed by factors such flight line noise. Figure 9 demonstrates additional contact points using the Analytical Signal (AS) approach. In comparison to other methods, this basement has the shallowest minimum and deepest maximum depths, at 0.01 km and 0.64 km, respectively.

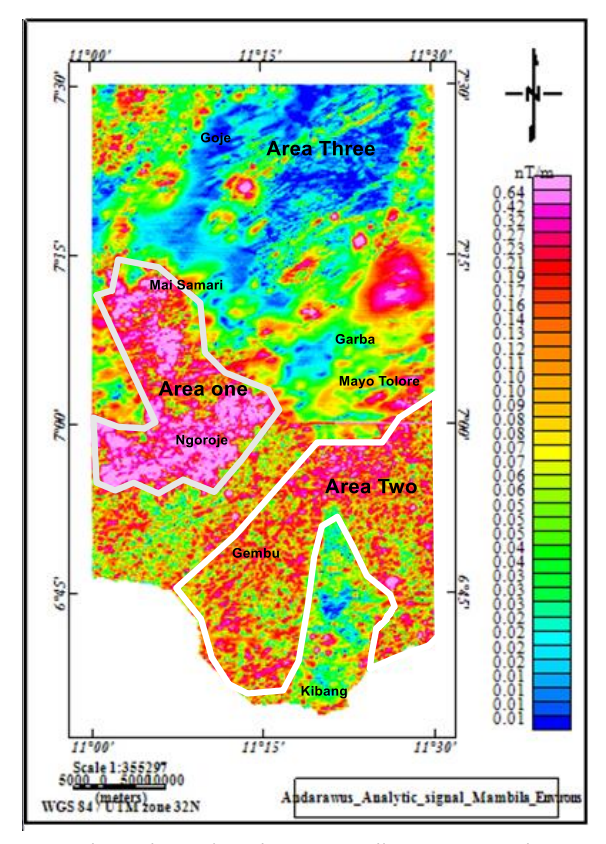


Figure 9: Total gradient (analytic signal) map over the study area

4.3.5. Horizontal derivatives (HDR)

Most of the structural components of the study including contacts, inferred faults, field, intrusions, and the form of some lithology to some extent, are shown in horizontal derivatives images (Okpoli and Akinbulejo, 2021). Horizontal gradient computations were applied to the RTE map in order to make the lithological contact boundaries more clear, even if the pseudogravity anomaly contour map is comparatively more useful in displaying the location of subsurface anomaly sources. The largest gradient will be localised precisely at the edge of the bodies since the maximum horizontal gradient of RTE anomaly data originating from subsurface rocks tends to be at the object's edge (Figure 10). By detecting

the abrupt lateral variations in rock magnetism, this can be used to determine the contact boundaries between the surrounding rocks and the basaltic lithology (Nurdiyanto et al., 2004). Figure 10 displays the contour of the horizontal gradient, with values ranging from 0.011 to -0.11nT. In the research region, the distribution pattern of the basaltic intrusion is represented by these lithological contact boundaries. Although there are a few minor variations, the distribution pattern of basaltic rocks generally agrees with the geology, satellite imaging, and pseudogravity maps. This discrepancy makes sense since the horizontal gradient map shows the surface and subsurface horizontal borders of basaltic intrusion (Blakely 1995).

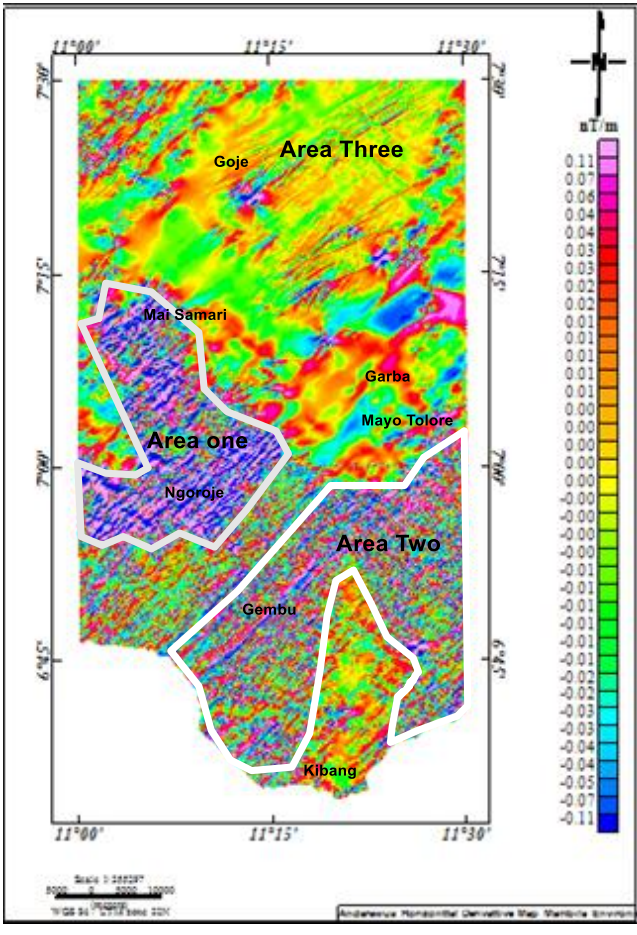


Figure 10: Horizontal derivative of magnetic data over Mambilla and environs

4.3.6. Pseudo-gravity transformation

While the pseudogravity anomaly map (Figure 11) provides more information about the location of subsurface anomaly sources, horizontal gradient computations can be used to define the limits of lithological contacts. Pseudogravity anomaly data (Figure 11) emanating from subterranean objects or rocks tend to have a maximum horizontal gradient at their edge, which causes the maximum gradient to be localised just at the object's edge as Figure 11 illustrates (Blakely 1995). By detecting the abrupt change in rock density in a lateral direction, this can be used to determine the contact boundaries between the surrounding rocks and the basaltic lithology (Nurdiyanto et al., 2004). The region's pseudo-gravity map was split into three sections:

high densities, ranging from 0.25 to 0.07 mg, intermediate densities, ranging from 0.06 to 0.01 mg, and low densities, ranging from -0.11 mg to -0.01 mg, respectively. The study area's pseudogravity map is displayed in Figure 11. As can be observed from the pseudogravity, landsat imagery, and geological maps, the comparatively high-density areas are linked to basaltic intrusions because of the high densities of basalts. There is a significant density of rocks in the study area's middle and southernmost regions. Geological literature (Asikin and Handoyo 1992) indicates that this is thought to be the centre of a very compact basaltic intrusion in the form of a dyke structure. While the low anomaly in the west, north, and east indicates the predominance of low density basement rocks

near the surface, the high anomaly in the south and central sections shows the intrusion of compact basaltic rocks close to the surface. Daya1 et al. (2021) reported that bauxite deposits mineralized these locations. With values ranging from 0.003 to 0.553 mGal, the two bauxite-bearing hills at the Mayo Sumsum and Gurgu regions measure 500 m x 1000 m and 300 m x 1000 m, respectively. The distribution pattern of the basaltic intrusion in the region is represented by these lithological contact boundaries. Although there are some minor variations, the distribution pattern of basaltic rocks generally agrees with the geology, landsat imagery, and

pseudogravity maps. This discrepancy makes sense as, according to Blakely (1995), the pseudogravity map illustrates the distribution pattern of basaltic intrusion both below and above the surface, but the geological map merely displays the distribution of basaltic rocks that are exposed at the surface. This basaltic rock not only penetrates from below but also intrudes the basement rocks. These rock units occur as sills and dyke structures in the field, which are intrusions with an elongated flat shape that are parallel and perpendicular to the plane of the rock strata (Sembiring et al., 2016).

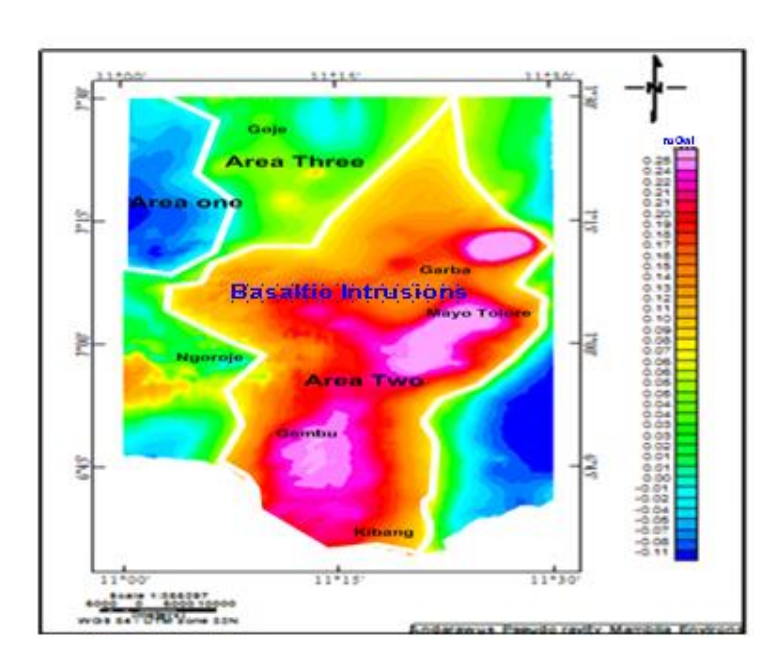


Figure 11: Pseudo-gravity transforms map of Mambilla and environs

4.3.7 Depth Estimation to buried magnetic sources

The power spectrum, a two-dimensional function of energy and wave number, can be used to estimate the typical depth of source assemblages (Spector & Grant, 1970). The radially averaged power spectrum or spectral plot displays all depth estimations to the top of the magnetic sources responsible for the observed anomalies in the study region (Figure 12). The gradient of the layers was calculated based on the wavelength of the magnetic sources. One of the magnetic sources has a gradient of 1.60 km, while another has a gradient of 4.47 km. Therefore, 0.28 km and 4.25 km are estimated to be the total depths to the top of the magnetic shallower and deeper sources in the area, respectively.

4.3.8. Spectral depth analysis

In Figure 4, we see the five retrieved profiles of the shaded relief anomaly relative to the magnetic equator along the rift axis of the research region. RTE anomaly profiles are analysed with 32 data points from spectral blocks using the one-dimensional power spectrum method. The estimated power spectrum is a logarithmic plot of spectral energy vs wave number. The top and shallow depths of a magnetic source can be calculated using the slope (gradient) of the power spectrum curve (deep and shallow interfaces). Linear curves

(from which slope values are derived) are fitted to power spectrum data using a piece-wise least-squares method. Low- and high-frequency weighted energy from the source origin are represented by the fitted lines, from which the gradients (slopes) are derived. The majority of this power comes from low-frequency sources, as shown in Figure 12(a-f). Source depth interfaces are categorised as shallow or deep based on the wave number (frequency) and slope (gradient) changes, as summarised in Table 1.

Along the rift axis of the convergence zone, the depth to shallow magnetic sources is around 1.5 km while the depth to deep magnetic sources is about 4.42 km. Mean depths to magnetic contrast interfaces are calculated, with two distinct interfaces being read and categorised as deep and shallow source depths (Table 1). Figures 15 and 16 are maps of the magnetic horizons in the research region. A value of r2 of 0.0002 is used to derive a shallow interface depth of about 23 m. Incorrect conclusions could be drawn if an r-squared value of 23 m were accepted as the source depth. This phenomenon is better understood as the results of terrain removal. Using the source depth estimation method, we mapped the magnetic horizons across the study area and generated two types of structural maps: deep and shallow (Figure 13 and 14).

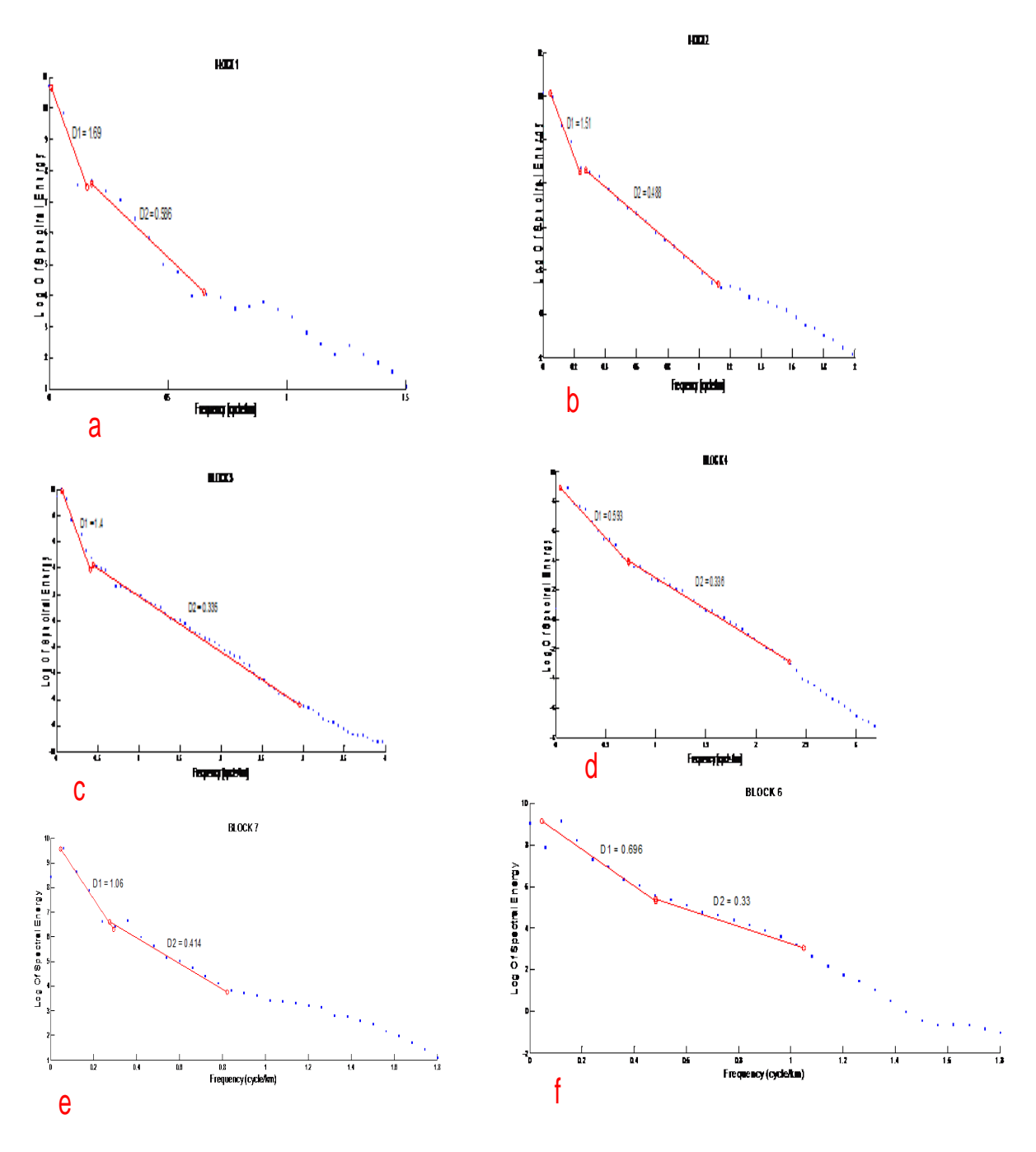


Fig. 12(a-f). Examples of spectral plot over Mambilla and environs

Table 1. Computed spectral analysis of the Mambilla sheet 295 of about 16 blocks in the study area

Sheet	S/No	Spectral	Longitude		Latitude		Spectral Depth (km)	
Name		Block						
			X1	X2	Y1	Y2	Deep	Shallow
							source(D1)	source(D2)
	1	1	11.0	11.125	7.375	7.5	1.69	0.586
	2	2	11.125	11.25	7.375	7.5	1.51	0.488
	3	3	11.25	11.375	7.375	7.5	1.40	0.335
	4	4	11.375	11.5	7.375	7.5	0.593	0.336
	5	5	11.0	11.125	7.25	7.375	3.6	1.17
	6	6	11.125	11.25	7.25	7.375	0.696	0.33
	7	7	11.25	11.375	7.25	7.375	1.06	0.414
	8	8	11.375	11.5	7.25	7.375	2.19	0.477
	9	9	11.0	11.125	7.125	7.25	1.28	0.335
	10	10	11.125	11.25	7.125	7.25	0.869	0.191
	11	11	11.25	11.375	7.125	7.25	0.994	0.234
	12	12	11.375	11.5	7.125	7.25	1.78	0.554
	13	13	11.0	11.125	7.0	7.125	1.14	0.232
	14	14	11.125	11.25	7.0	7.125	4.42	0.529
	15	15	11.25	11.375	7.0	7.125	1.41	0.304
	16	16	11.375	11.5	7.0	7.125	3.72	0.856
Average							1.772	0.461

Table 2. Computed spectral analysis of the Gashaka sheet 276 of about 16 blocks in the study area.

Sheet Name	S/No	Spectral Block	Longitude		Latitude		Spectral Depth (km)	
Mambilla295			X1	X2	Y1	Y2	Deep	Shallow
							source(D1)	source(D2)
	1	17	11.0	11.125	6.875	7.0	0.583	0.281
	2	18	11.125	11.25	6.875	7.0	0.56	0.179
	3	19	11.25	11.375	6.875	7.0	1.39	0.451
	4	20	11.375	11.5	6.875	7.0	1.39	0.422
	5	21	11.0	11.125	6.75	6.875	4.06	0.608
	6	22	11.125	11.25	6.75	6.875	1.91	0.537
	7	23	11.25	11.375	6.75	6.875	0.749	0.328
	8	24	11.375	11.5	6.75	6.875	2.29	0.323
	9	25	11.0	11.125	6.625	6.75	0.157	0.062
	10	26	11.125	11.25	6.625	6.75	0.551	0.28
	11	27	11.25	11.375	6.625	6.75	0.996	0.541
	12	28	11.375	11.5	6.625	6.75	1.79	0.546
	13	29	11.0	11.125	6.5	6.625	NA	NA
	14	30	11.125	11.25	6.5	6.625	0.903	0.278
	15	31	11.25	11.375	6.5	6.625	0.931	0.222
	16	32	11.375	11.5	6.5	6.625	0.354	0.11
Average							1.241	0.345

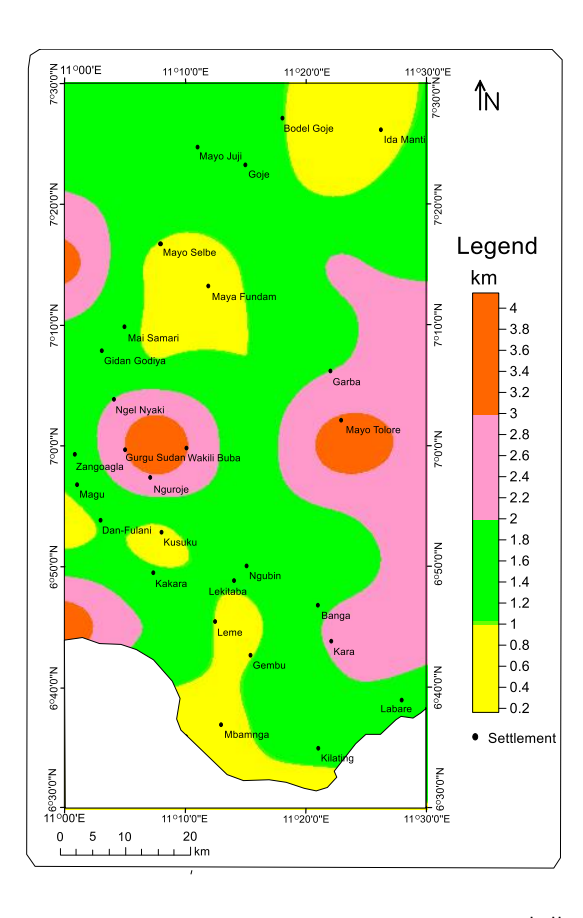


Figure 13: Magnetic Source to Deeper Sources over Mambilla and Environs

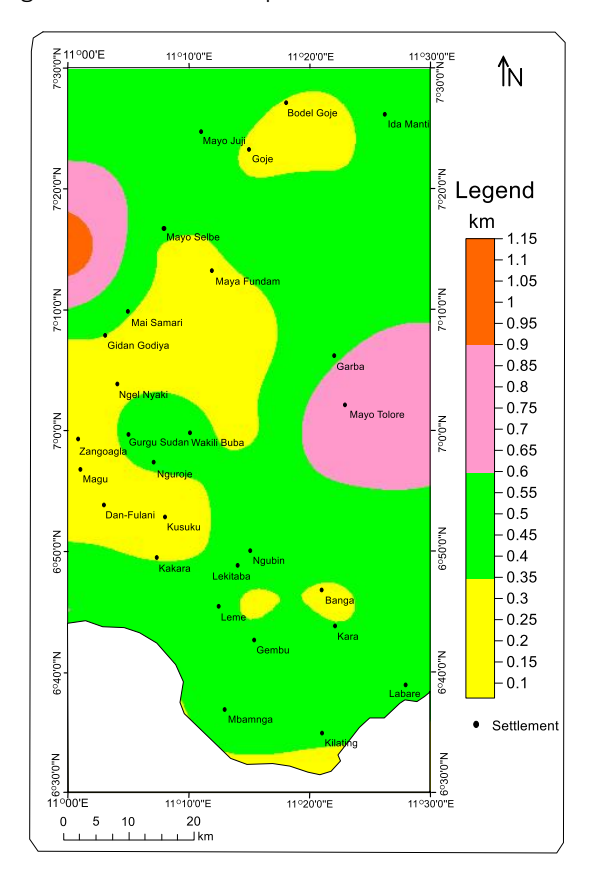


Figure 14: Magnetic Source to Shallow Sources over Mambilla and Environs

4.3.9. Source parameter imaging (SPI)

The method of Source Parameter Imaging was used to measure the distance to magnetic sources (SPI). The depth variation of different magnetic sources is highlighted on the SPI map (Figs. 15). The depth of various magnetic sources is shown in the corresponding legend. Depths with positive values are receptive to magnetic fields, whereas those with negative values are magnetically quiescent. However, these numbers illustrate the basement's undulating nature and the precise meter-level positioning of the

magnetic sources within the research area. According to the SPI map, the study area's highest depth is located in the north and east, while the study area's minimum depth is concentrated in the south. The SPI approach locates magnetic sources as deep as 3780.40m below the surface. The depth range of 52.90m to 3780.40m measured by SPI is consistent with the depth range determined by spectral analysis and other sources. The predominant NNE-SSW tectonic tendencies support the quantitative result (Likkason et al, 2013).

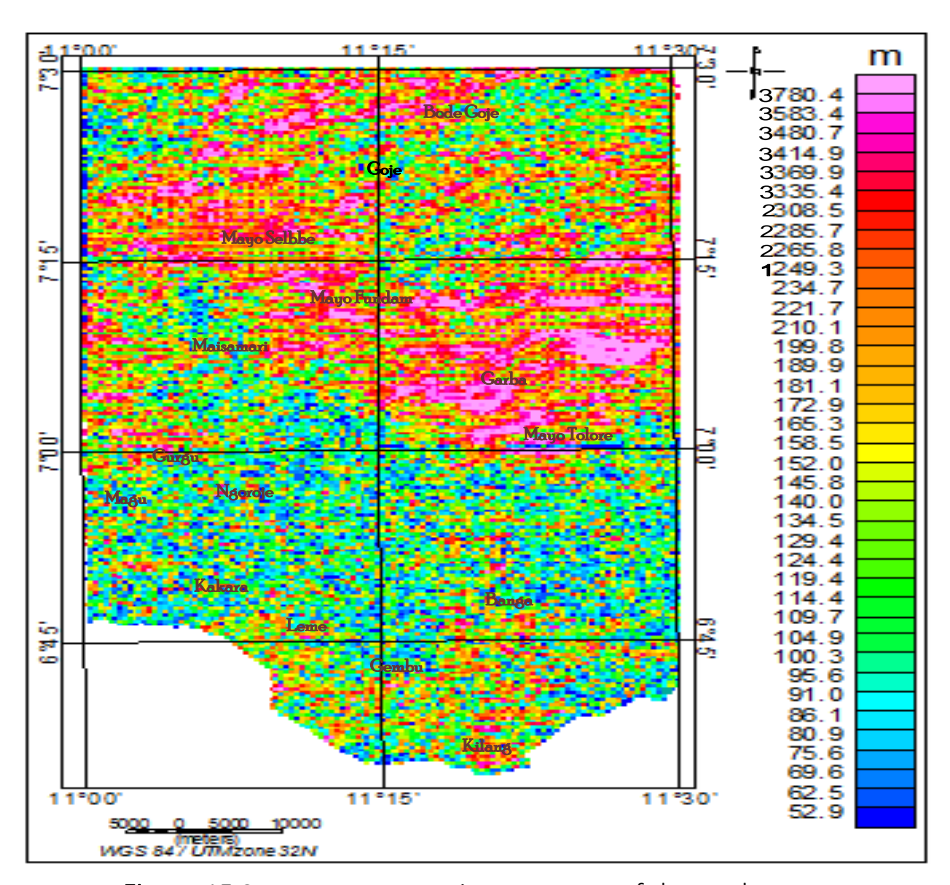


Figure:15 Source parameter imagery map of the study area.

Conclusions

At the Mambilla Plateau and its surroundings, integrated geophysical analysis was used to pinpoint the position and patterns of basaltic intrusion. Whereas the principal component analysis of the Landsat 8 ETM+ image (PC2, PC1, PC4 in R, G, and B) of the study area identified rocks such as younger basalt (yb), porphyritic

granite (pg), granite gneisses (Gn), and migmatite gneisses (Mg), the Landsat-8 ETM+ false colour composite image (bands 7, 4, 2 in R, G, and B) identified rocks such as these. Total magnetic intensity map a had minimum and maximum values of 33030.343nT and 33172.792nT, respectively, with a mean variation of 33068.89nT and 31.50nT. The average value of

the main magnetic field map is 33293.4495 nT, with values ranging from 33228.522 nT to 33358.377 nT. The average value of the crustal magnetic field map, caused by localised ore bodies or intrusions, is -159.50 nT, with values ranging from -397.669 nT to -80.699 nT. The RTE values throughout the region range from -82.382nT to -392.122nT, indicating areas with faults, fractures, and geological intrusions. The magnetic equator field map was reduced and extended upward for a distance of 15 km, displaying values that varied between -279.141 nT and -157.160 nT. The residual magnetic bodies and surface lineaments in remote sensing data follow the NNE-SSW and NE-SW directions, the prominent structural trends of deep sources stretch mostly in the NE-SW and NW-SE directions with minor N-S, NNW-SSE. The area's pseudo-gravity map showed three distinct zones: low densities ranged from -0.11 to -0.01mGal, while high densities were found between 0.25mGal and 0.01mGal, indicating places with moderate to intermediate densities. The edge of the object is typically where the largest horizontal gradient of RTE anomalies data originating from subsurface rocks is found, allowing the maximum gradient to be directly localised to map boundaries of the distinct lithologies. This was used to determine the contact boundaries between the surrounding rocks and the basaltic intrusion, faults, mineralization, etc. by detecting the abrupt changes in rock magnetism in a lateral direction. Using power spectral and source parameter imagery magnetic depth estimation, two source depths of 0.28km and 4.42 km were determined.

References

Abraham, E.M.,

and M.A. Owens. (2019). Modeling subsurface geologic structures at the Ikogosi geothermal field, Southwestern Nigeria, using gravity, magnetics, and seismic interferometry techniques. *Journal of Geophysics and Engineering* 16, no. 4: 729–41

Abdelnasser, A., Kumral, M., 2017. The nature of gold-bearing fluids in Atud gold deposit, Central Eastern Desert, Egypt. Int. Geol. Rev. 59 (15), 1845–1860. https://doi.org/10.1080/00206814.2017 .1299043.

Abo-Ezz E.R. and EssaK.S.,(2016). A least-squares minimization approach for model parameters estimate by using a new magnetic anomaly formula, Pure and Applied Geophysics 173,1265-1278.

Afolabi, O.A., Oduneye, O.C., Olatunji, A.S., Ajibade, A.C., 2020. Understanding Precambrian Komatiite Petrochemistry from talc bodies within the Ilesha Schist belt, Southwestern Nigeria. Ife Journal of Science. 2020; 21 (3):107–107. Available from:

https://dx.doi.org/10.4314/ijs.v21i3.10.

Anudu GK, Stephenson RA, Macdonald DIM.
Using high-resolution aeromagnetic data
to recognize and map intra-sedimentary
volcanic rocks and geological structures
across the Cretaceous middle Benue
Trough, Nigeria. J Afr Earth Sci.
2014;99:625–36.

- Asikin, S., and Handoyo, A., (1992). *Geological Map of Banyumas Sheet, Java, Scale 1:* 100.000. Center for Geological Research and Development, Bandung.
- Auckland University (2019). Geology Rock and Mineral; Basalt, Available: https://flexiblelearning.auckland.ac. nz/rocks_minerals/rocks/basalt.html, November 17.
- Azizi, M., Saibi, H., & Cooper, G. R. J. (2015).

 Mineral and structural mapping of the Aynak-Logar Valley (eastern Afghanistan) from hyperspectral remote sensing data and aeromagnetic data. Arabian Journal of Geosciences, 8, 10911-10918.

 https://doi.org/10.1007/s12517-015-1993-2
- Baranov, V. (1957). A new Method for interpretation of Aeromagnetic Maps:
 Pseudo-gravimetric anomalies:
 Geophysics, Vol.22, pp 359–383.
- Blakely, R.J. (1995). Potential Theory in Gravity and Magnetic Applications. Cambridge Univ. Press. 199, 464pp.
- Cordell, L. and Grauch, V.J.S. (1982) Mapping Basement Magnetization Zones from Aeromagnetic Data in the San Juan Basin, New Mexico. SEG Technical Program Expanded Abstracts, 246-247.
- Daya, A.M, Ahmad,I.H, Abubakar S. M, and Isah.Y(2021). Geology and Possible Host for Bauxite Mineralization of Mambila Plateau, NE Nigeria. International Journal of Geo-informatics and Geological Science, Volume 8 Issue 3, 22-28. /doi:10.14445/23939206/IJGGS-V8I3P104

- Ekwok S.E, Akpan AE, Ebong DE (2019)
 Enhancement and modelling of
 aeromagnetic data of some inland
 basins, southeastern Nigeria.JAfr Earth
 Sci 155:43–53
- Essa K.S. and Elhussein M., (2017). A new approach for the interpretation of magnetic data by a 2-D dipping dike, Journal of Applied Geophysics 136 431–443.
- Essam, A., Ahmed, S., Keisuke Ushijima. (2003).Interpretation of aeromagnetic data of Gebel El-Zeit area, Gulf of Suez, Egypt using magnetic gradient techniques. *Memoirs of Faculty of Engineering,Kyushu University*. 63 (3): 139-149.
- El-Desoky, H.M., Shahin, T.M., Amer, Y.Z., 2021.
 Characteristic of gold mineralization associated with granites at Hamash old gold mine, South Eastern Desert, Egypt.
 Arab. J. Geosci. 14 (7).
- Farrand, W.H., Harsanyi, J.C., 1997. Mapping the distribution of mine tailings in the Coeur d'Alene River Valley, Idaho, through the use of a constrained energy minimization technique. Remote Sens. Environ. 59, 64–76.
- Feumoe A N S, Ndougsa-Mbarga T, Manguelle-Dicoum E and Fairhead J D (2012), "Delineation of Tectonic Lineaments Using Aeromagnetic Data For the South-East Cameroon Area, *GEOFIZIKA*, Vol. 29.

- Ganas, A., Pavlides, S., Karastathis, V., 2005.

 DEM-based morphometry of rangefront escarpments in Attica, central Greece, and its relation to fault slip rates.

 Geomorphology 65 (3-4), 301–319.
- Goetz, A.F.H., Rock, B.N., Rowan, L.C., 1983. Remote sensing for exploration: an overview, Econ. Geol. 78, 573-590.
- Geomatics(PCI) Enterprises Inc, 2015. geospatial image processing software. www.pcigeomatics.com..
- Harsanyi, J.C., (1993). Detection and classification of subpixel spectral signatures in hyperspectral image sequences Unpublished Ph.D. Thesis. University of Maryland, p. 116.
- Helmy, M., Reinhard, K., Fritz, H., Loizenbauer, J., (2004). The Sukari Gold Mine, Eastern Desert-Egypt: structural setting, mineralogy and fluid inclusion study.Mineral. Deposita 39, 49.
- Jeje L.K (1983). Aspects of geomorphology of Nigeria. Heinemann educational books.
- Kebede, H., Alemu, A., & Fisseha, S. (2020).

 Upward continuation and polynomial trend analysis as a gravity data decomposition, case study at Ziway-Shala basin, central Main Ethiopian rift. Heliyon, 6(1), e03292. https://doi.org/10.1016/j.heliyon.2020.e 03292
- Kearey, P., Brooks, M. and Hill, I., 2002. *An introduction to geophysical exploration*.

 1st ed. Malden, MA: Blackwell Science.
- Klemm, R., Klemm, D., 2013. Gold and gold mining in anceint Egypt and Nubia. Springer. https://doi 10.1007/978-3-642-22508-6.

- Likkason, O. K, Singh, G.P, and N. K. Samaila, N. K. (2013). A Study of the Middle Benue Trough (Nigeria) Based on Geological Application and Analyses of Spectra of Aeromagnetic Data. Energy Sources, Part A, 35:706–716. Copyright © Taylor & Francis Group, LLC ISSN: 1556-7036 print/1556-7230 online DOI: 10.1080/15567036.2010.514588.
- Likkason. O. K (2014). Exploring and Using the Magnetic Methods. http://dx.doi.org/10.5772/57163
- Lyatsky, H., 2010. Magnetic and Gravity Methods in Mineral Exploration: the Value of Well-Rounded Geophysical Skills
- Mammo, T. (2012). Analysis of gravity field to reconstruct the structure of Omo basin in SW Ethiopia and implications for hydrocarbon potential. Marine and Petroleum Geology, 29(1), 104-114. https://doi.org/10.1016/j.marpetgeo.20 11.08.013
- Macleod, I.N., Jones K., Dai, T.F. (1993). 3-D analyticsignal in the interpretation of total magnetic field data at low magnetic latitude, *Proceedings of the Third International Congress of Brazilian Society of Geophysics*. https://doi.org/10.1071/EG993679
- Mould .A.W. S (1960). Report on a rapid reconnaissance soil survey of the Mambilla plateau. Bulletin 15, Soil survey section, regional research station, ministry of agriculture, Samaru, Zaria.

- Mubi AM, Tukur. A.L (2005). Geology and relief of Nigeria. Nigeria. Heinemann educational books.
- Nikolakopoulos, K.G., Kamaratakis, E.K., Chrysoulakis, N., 2006. SRTM vs ASTER elevation products. Comparison for two regions in crete, Greece. Int. J. Remote Sens.. 27 (21), 4819–4838.
- Nurdiyanto, B. S., Wahyudi, Suyanto, I., Magnetic
 Data Analysis to Determine the
 Subsurface Structure of the Hot Water
 Manifestation Area on the North Slope of
 Ungaran Volcano, *Proceedings of the Indonesian Geophysicists Association*,
 29th Annual Scientific Meeting,
 Yogyakarta, October 5-7, 2004.
- Okpoli, C.C., Imo, V., (2019). Exploration for mineralization and hydrocarbon prospecting zones of Abakiliki aspect of lower Benue trough. ActaScientifica Malaysia (ASM) 3 (2),

12-16.

- Okpoli, C.C., Akingboye, A.S., (2019). Application of high-resolution gravity data for lithostructural and depth characterisation around Igabi area. Northwestern Nigeria-NRIAG Journal of Astronomy and Geophysics 8 (1), 231–241.
- Okpoli, C.C., Eyitoyo, F.B., (2016). Aeromagnetic study of Okitipupa region. Southwestern Nigeria, International Basic and Applied Research Journal 2 (7), 1–20.
- Okpoli, C.C., Akinbulejo, B.O., (2021).

 Aeromagnetic and electrical resistivity
 mapping of groundwater development

- around Ilesha schist belt, southwestern Nigeria. J. Pet. Explor. Prod. Pp15
- Phillips, J.D. (2000) Locating Magnetic Contacts:
 A Comparison of the Horizontal Gradient,
 Analytic Signal, and Local Wavenumber
 Methods: Society of Exploration
 Geophysicists. Abstracts with Programs,
 Calgary, 2000.
- Pour, A.B., Hashim, M., Hong, J.K., Park, Y., 2019. Lithological and alteration mineral mapping in poorly exposed lithologies using Landsat-8 and ASTER satellite data: north-eastern Graham Land, Antarctic Peninsula. Ore Geol. Rev. 108, 112–133.
- Roest, W. R., Verhoef, J., & Pilkington, M. (1992).

 Magnetic interpretation using the 3-D analytic signal. Geophysics, 57(1), 116-125. https://doi.org/10.1190/1.1443174
- Salem, A., Williams, S., Fairhead, J. D., Ravat, D., & Smith, R. (2007). Tilt-depth method: A simple depth estimation method using first-order magnetic derivatives. The leading edge, 26(12), 1502-1505. https://doi.org/10.1190/1.2821934
- Smith, R. S., Thurston, J. B., Dai, T. F., & MacLeod,
 I. N. (1998). iSPITM the improved source parameter imaging method.
 Geophysical prospecting, 46(2), 141-151.
 https://doi.org/10.1046/j.1365-2478.1998.00084.x
- Sembiring, R.R., Sunarwan, B., Syaiful, M., (2016).

 Geology and Study of Turbidite Deposits
 in Ciwuni and Surrounding Areas,
 Kesugihan District, Cilacap Regency,
 Central Java, Jurnal Online Mahasiswa
 (JOM) Geological Engineering Section,
 vol. 1, no. 1, pp. 1-14.

- Spector, A., and Grant, F.S., 1970. Statistical models for interpreting aeromagnetic data. Geophysics, vol 35 pp 293-302.
- Subarsyah S and Priohandono YA 2016 Metoda Pseudo-Gravity DalamAnalisisKelurusan Dan Patahan Di SekitarTinggianAsahan, PerairanSelatMalaka. *J GeolKelaut***7(2)** p.65–71
- Süzen, M.L., Toprak, V., 1998. Filtering of satellite images in geological lineament analyses: an application to a fault zone in Central Turkey. Int. J. Remote Sens. 19 (6), 1101–1114.
- Tanaka, A., Okubo, Y. and Matsubayashi, O.(1999). Curie point depth based on spectrum analysis of the magnetic anomaly data in east and southeast Asia. Tectonophysics 306, 461-470.
- Tanaka, A., Okubo, Y. and Matsubayashi, O.(1999). Curie point depth based on spectrum analysis of the magnetic anomaly data in east and southeast Asia. Tectonophysics 306, 461-470.
- Telford, W. M., Gedaart, L. P, Sheriff, R. E.,(1990).

 Applied Geophysics, Cambridge University Press, Cambridge
- Thomson, D.J. (1982) Spectrum Estimation and Harmonic Analysis. Proceedings of the IEEE, 70, 1055-1096. https://doi.org/10.1109/PROC.1982.124 33

- Thurston, J.B. and Smith R.S. (1997). Automatic conversion of magnetic data to depth, dip and susceptibility contrast using SPI method, Geophysics. 62(3): 807-813.
- Tukur, A. L, Adebayo. A. A, Galtima A (2005). The land and people of the Mambilla Plateau, Nigeria. Heinemann educational.
- Udensi, E. E., Osazuwa I. B. and Daniyan, M. A. (2003). Trend analysis of the total magnetic field over the Bida Basin, Nigeria. Nigerian Journal of Physics. 15,143–151.
- Werner, F. (1953). Interpretation of magnetic anomalies at sheet likes bodies. Geological Understanding Series, CC Arabok, 43(6), 66-97.